Liu, Yunpeng, Zhu, Jinwei, Wang, Zhenyu, Yan, Xuanye, Zhang, Juantao, Zhang, Wenlong, Xu, Hao, Marken, Frank, Feng, Jiangtao, Hou, Bo , Yan, Wei, Li, Mingtao and Ren, Zijun 2022. Towards energy level cascaded “quantum armours” combating metal corrosion. Applied Surface Science 593 , 153369. 10.1016/j.apsusc.2022.153369

Publishers page: http://dx.doi.org/10.1016/j.apsusc.2022.153369

Towards Energy Level Cascaded “Quantum Armours” Combating Metal Corrosion

Yunpeng Liu [a], Jinwei Zhu [a,e], Zhenyu Wang [a], Xuanye Yan [a], Juantao Zhang [a], Wenlong Zhang [a], Hao Xu [a], Frank Marken [b], Jiangtao Feng [a*], Bo Hou [c**], Wei Yan [d***] , Mingtao Li[g], and Zijun Ren [f]

a Department of Environmental Science & Engineering, State Key Laboratory of Multiphase Flow in Power Engineering, School of Energy and Power Engineering, Xi’an Jiaotong University, Xi’an, 710049, China. Email: fjtes@xjtu.edu.cn
b Department of Chemistry, University of Bath, Claverton Down, Bath BA2 7AY, U.K.
c School of Physics and Astronomy, Cardiff University, The Parade, Cardiff, CF24 3AA, Wales, UK. Email: HouB6@cardiff.ac.uk
d State Key Laboratory of Multiphase Flow in Power Engineering, School of Energy and Power Engineering, Xi’an Jiaotong University, Xi’an, 710049, China. Email: yanwei@xjtu.edu.cn
e Shaanxi Electrical Equipment Institute, Xi’an, 710025, China
f Instrument Analysis Center of Xi’an Jiaotong University, Xi’an Jiaotong University, Xi’an, 710049, China
g International Research Center for Renewable Energy (IRCRE), State Key Laboratory of Multiphase Flow in Power Engineering (MFPE), Xi’an Jiaotong University, Xi’an, 710049, China

Corresponding authors:
Jiangtao Feng: fjtes@xjtu.edu.cn
Bo Hou: HouB6@cardiff.ac.uk
Wei Yan: yanwei@xjtu.edu.cn

Abstract: Stainless steels typically feature high toughness and good corrosion resistance. However, pitting corrosion can easily occur on stainless steel and the passivation film tends to be vulnerable under pressure or in brine environments. Metal corrosion is a long-standing challenge for the steel industry, forging a path to net-zero. Herein, by successive growth of a series of quantum confined nanocrystals such as quantum dots and nanorods with gradient band energy level alignment, high-performance photoelectrochemical cathodic protection for steel is demonstrated with remarkable mechanical and electrochemical stability. Under simulated solar light illumination, effective photoinduced protection can be realized for 304 stainless steel which enables long-term corrosion resistance in a 3.5 wt% NaCl solution. Unique nanotree-like structures and the quaternary material combination can store excess charges and release them gradually, enabling time-delay protection for metals after light excitation. Various promising functionalities as unique photoelectrodes can be envisioned arising from the proposed 3D nanotree morphology.

Keywords: quantum dot, cascaded-junction, 304 stainless steel, photoelectrochemical cathodic protection, DFT

Introduction

Corrosion resistance will play a significant role in our future daily lives when approaching carbon neutrality and improved sustainability. Many metal-based engineering objects are required to last for at least 60 years to meet the global “Clean Growth” demands. However, day after day resisting damage from a corrosive, watery world under conditions of extreme temperatures, pressures, or ionizing radiation, can lead to enhanced corrosion. The passivation film of stainless steel tends to be vulnerable, particularly in brine environment.[1] This problem affects nuclear reactors but also thousands of wastewater steel tanks.[2] Metal corrosion presents a global challenge confronting international industrial development, causing enormous waste/economic losses and threatening our sustainable development roadmaps. For instance, the annual world economy lost in metal corrosion is equivalent to 3.34% of the global GDP.[3] Many approaches have been improved to deal with this issue, including corrosion inhibitors,[4] anti-corrosion coatings,[5] and electrochemical protection.[6] Photoelectrochemical cathodic protection (PCP) has attracted attention over the past few years due to being environmentally friendly, grid-independent, and more sustainable.[7]

PCP is a promising cathodic protection approach for open light-exposed structures, providing continuous photoinduced electrons to the metal to make the metal’s surface potential. Expanding the absorption spectral region of photoanode materials makes a critical contribution to advancing PCP efficiency.[8] Carefully designed nanomaterials can help improve efficiency. An important issue to be resolved is to maintain protection during the night.

TiO_2 has been employed previously as PCP material owing to its chemical stability and low cost.[9] Especially, one-dimensional (1D) TiO_2 nanorods (TNRs) display good PCP efficiency resulted from the 1D structure hindering the recombination of e^-/h^+ pairs.[10] Nevertheless, the large bandgap (> 3 eV) of TiO_2 is linked to a weakly photoresponse to solar light.[11] Several methods, including doping,[12] noble metal particle decoration,[13] hydrogenation treatment[14] and heterostructure construction,[15] have been employed to improve the light absorption of TNRs. The combination of TNRs with a narrow bandgap material to form a type-II heterojunction has been demonstrated to be the most efficient approach.[16]

CdS has been utilized as an efficient PCP material with a smaller bandgap than TiO_2 and higher light absorption efficiency. Zhang et al.[17] and Li et al.[18] demonstrated that CdS particles-modified 1D TiO_2 nanotubes array film exhibited good PCP efficiency under white light illumination. Due to the size-dependent quantum confinement effect, CdS quantum dots (QDs) have received considerable interest in the last decades.[19] However, CdS QDs exhibited inferior photo-corrosion resistance.[20] Mn^{2+} doped CdS QDs (Mn-CdS QDs) have been proposed and proven to be better at avoiding the oxidation of S^{2-} to extend the lifetime of the photo-produced charge carriers.[21] The Mn-CdS QDs/TNRs photoanode has recently been adopted in various photoelectrochemical (PEC) systems.[22] Therefore, this system could be a good candidate for PCP application.

Abundant grain boundaries usually impede long-range charge transfer.[23] The recombination rate of photogenerated carries can be very high when 0D materials (such as QDs) stack directly on the 1D TNRs film. Furthermore, the vertically grown nanorods limit suitable deposited sites, leading to lower QDs loading and lower solar light absorption.[24] Therefore, it is important to seek the appropriate TNRs-based substrate to accommodate more Mn-CdS QDs and form a better photoanode.

Hierarchical hetero-structured TiO_2 nanotree arrays represent a new type of TNRs that consists of 1D rutile TiO_2 nanorods as trunks and 3D anatase TiO_2 nanorods as branches.[25] The high surface-to-volume ratios of the 3D anatase TiO_2 branches could provide sufficient loading sites for accommodating more Mn-CdS QDs.[24]. Therefore, due to the cascaded band-edge alignment between rutile/anatase interface and enlarged light-harvesting surface area, this heterophase nano-structure has exhibited an excellent photoconversion efficiency in PEC systems.[26] Some reports also introduced hydrogenated-TiO_2 as a "bark" layer on the 3D rutile/anatase TiO_2 nanotree array to further enhance the photoconversion efficiency.[11] Hydrogenation treatment could generate oxygen vacancies (Ov) and free state Ti^{3+} cations, forming additional impurity energy levels to enhance sub-bandgap optical absorption.[27] The presence of surface lattice disorder from the hydrogenated TNR layer has a negligible effect on the 1D photocarrier transmission pathway from the embedded rutile/anatase TiO_2 nanotree arrays.[28] Given the potential of the 3D rutile/anatase TiO_2 nanotree array, there may be potential for applying this hierarchical rutile/anatase TiO_2 nanotree array to achieve improved PCP performance, however, sunch superstructural materials enhanced PCP hasn't been reported so far which may result from materials growth challenges.

Herein, a new material based on quaternary Mn-***C***dS QDs/***A***natase TiO_2 branches/***H***ydrogenated-***T***iO_2 layer/***TNRs*** (CAHT NRs) with a nanotree-like superstructure morphology (Scheme 1) is fabricated, which exhibits much higher PCP performance when applied to 304 stainless steel (304SS) compared to similar data obtained with previously reported binary and ternary systems. Using a four-step synthesis process including hydrothermal reaction, hydrogenation treatment, successive ionic layer adsorption and reaction (SILAR) method, CAHT NRs can be successfully prepared with good morphology and controlled structure. Comprehensive characterizations of new material reveals crystal structure, surface morphology, chemical composition, optical properties, ensuring the successful growth of this quaternary structure. Besides typical PCP analysis, we also systematically characterize the PCP after turning off the light to explore the possibility of maintaining protection during the night. DFT calculations were carried out to investigate the relationship between the unique multi-dimensional design and the high PCP performance.

Results and discussion

Structural characteristics

The XRD patterns of the TNRs, H-TNRs, A-H-TNRs and quaternary CAHT NRs films are shown in Figure 1a. The diffractogram shows rutile TiO_2 characteristics with diffraction peaks arising from the (1 1 0), (1 0 1), (1 1 1), (0 0 2), (3 0 1) and (1 1 2) reflections (JCPDS Card No. 65-0912) and the other peaks could be attributed to the FTO glass, which don't need to be deducted via grazing incidence XRD or shovel from substrate, due to the absence of SnO_2 in composite. No detectable difference between the curves of the pristine TNRs and H-TNRs can be resolved, which indicates hydrogenation reaction at 450 °C has a negligible effect on the crystal structure of rutile-TiO_2.[29] After the secondary hydrothermal growth of the anatase-TiO_2 branches, characteristic anatase (1 0 1) diffraction peak at ~25.2° (JCPDS No. 21-1272) emerged,[30] which indicates the formation of the anatase/hydrogenated layer/rutile-TiO_2 heterojunction. The peak intensity of A-H-TNRs at ~37.8° (corresponded to FTO substrate) [31] is higher than that of H-TNRs, which can be attributed to the reflection arising from the newly formed (0 0 4) plane (at 37.8°) of anatase TiO_2.[11] Note that no diffraction peaks from Mn-CdS QDs can be resolved on CAHT NRs composite film because the convolution of their broad diffraction patterns merged into main TiO_2 diffraction peaks.[32]

The Raman spectra of the TNRs, H-TNRs, A-H-TNRs and quaternary CAHT NRs films were employed to study the composition-dependent lattice variation.[33] In

Figure 1b, the curve of TNRs shows three characteristic peaks at about 230, 443 and 606 cm^{-1}, corresponding to the B_{1g}, E_g, A_{1g} modes of rutile TiO_2, respectively.[34] After hydrogenated treatment, the characteristic Raman peaks of rutile TiO_2 exhibit redshift and peak intensity reduction, resulting from nonstoichiometric and phonon confinement caused by the presence of Ti^{3+}.[35] Meanwhile, in the case of A-H-TNRs, there are two peaks at 398 and 516 nm, corresponding to the B_{1g} and A_{1g}+B_{1g} modes of anatase TiO_2,[36] which indicates the hybrid phases are successfully synthesized after a two-step hydrothermal reaction. A new peak at 300 nm could be resolved, corresponding to the 1LO modes of as-deposited CdS QDs.[37] It should be noted that the presence of the trace amount of Mn^{2+} dopant needs to be confirmed by more sensitive techniques such as Energy-dispersive X-ray sectors (EDS) and X-ray photoelectron spectroscopy (XPS), which will be provided in the latter discussion.

The morphologies of TNRs, H-TNRs, A-H-TNRs and quaternary CAHT NRs composite films were investigated by scanning electron microscope (SEM) under the same magnification. As displayed in Figure 2a, symmetrical and compact TNRs are perpendicularly grown on the FTO glass with a diameter of ~150 nm, which is consistent with our previous report.[38] After hydrogenated treatment (Figure 2b), no noticeable morphology and size variation of H-TNRs can be resolved. Via secondary hydrothermal treatment (Figure 2c), the trunks of A-H-TNRs were entirely covered by ~140 nm length nanoneedle-like branches being consistent with the previous literature.[39] Therefore, the rutile TiO_2 nanorod could serve as the trunk part of the nanotree, and the anatase TiO_2 nanoneedle could serve as the branch part of the nanotree, which enables more Mn-CdS QDs attachment (Figure 2d) for improving the PEC activity.[26] It should be noted that the cross-sectional view (Figure S1) of the CAHT NRs confirm the nanotree structure is still vertical on the FTO glass after Mn-CdS QDs decoration, which ensures the rapid spatial separation of photogenerated carriers from their 1D radial depletion layers.[40]

The microstructure of quaternary CAHT NRs films was further studied by Transmission electron microscopy (TEM) and high-resolution TEM (HRTEM). As displayed in Figure 3a, the representative 3D nanotree structure of CAHT NRs film can be discovered. Figure 3b shows a disordered layer with a thickness of ~5 nm present on the surface of the rutile TiO_2 nanorod, denoted as the "bark" layer of the nanotree. Reports have shown that such an amorphous layer contains plenty of Ov, improving the electrical conductivity and PEC reactivity of TNRs.[41] Furthermore, the 0.32 nm interplanar spacing could be clearly assigned to the rutile TiO_2 (1 1 0) plane, which prove the suitable growth along with the [0 0 1] zone axis.[42] Meanwhile, anatase-TiO_2 (1 0 1) planes with a lattice spacing of 0.35 nm can be resolved,[43] which indicates that the anatase-TiO_2 branches were successfully fabricated on the surface of rutile-TiO_2 layers. As shown in Figure 3c, it can be seen that the distribution of Mn-CdS QDs on the surface of anatase-TiO_2 branches is homogeneous without any agglomeration. The particle size was estimated to be ~6 nm. As shown in Figure 3d, the lattice fringes of 0.24 nm and 0.34 nm can be resolved, which corresponds to (1 0 2) and (0 0 2) planes of wurtzite-phase CdS.[44] In addition, as shown in the EDS elemental mapping images of CAHT NRs (Figure S2), Ti and O elements are concentrated in the center. In contrast, Cd, S and Mn elements are evenly distributed on the surface of the CAHT NRs samples.

Figure 4 display the XPS spectra of as-prepared composites which are utilized to study their chemical composition. Figure 4a shows the full scan survey XPS spectrum of the CAHT NRs film, displaying Ti 2p, O 1s, Cd 3d, Mn 2p, S 2p and C 1s peaks. As displayed in curves (I) of Figure 4b, the Ti 2p XPS spectrum of TNRs could be decomposed into two peaks (Ti $2p_{1/2}$ and Ti $2p_{3/2}$).[45] After hydrogenation treatment, the two characteristic peaks shift to a negative value by 0.6 eV compared with that of pristine TNRs, indicating the formation of Ti^{3+} on the surface of the H-TNRs sample [12]. Then, the successive positive shift of Ti $2p_{1/2}$ and Ti $2p_{3/2}$ peaks from curve (I) to curve (IV), demonstrate the existence of charges transfer among Mn-CdS QDs, anatase-TiO_2 branches, disordered layer and rutile-TiO_2 nanorods.[46] The high-resolution O 1s XPS spectrum for all samples can be divided into two peaks, as shown in Figure 4c. The dominant peak at 529.6 eV, could been attributed to the metal-oxygen bonds (Ti-O-Ti).[47] Also, the other oxygen-containing shoulder peak at 531.3 eV is assigned to the surface hydroxyl group (Ti-OH) [48] and the relevant difference of their binding energy fit nicely with the previous studies about hydrogenated TiO_2.[28] By calculating the peak area ratio (Ti-OH: Ti-O-Ti) from the four samples (approximately 0.019 in TNRs, 0.456 in H-TNRs, 0.304 in A-H-TNRs and 0.406 in CAHT NRs), we found the population of surface hydroxyl groups on H-TNRs is increased, which indicates the additional interstitial hydrogen incorporated into TiO_2 surface. Meanwhile, the downtrend of the surface hydroxyl groups from H-TNRs to A-H-TNRs is also detected because the continuous loads hinder the XPS signal collection, demonstrating the reduction of relevant Ti^{3+} concentration.[49] Interestingly, the increased concentration of Ti-OH on CAHT NRs surface is observed because of the surface hydration during the SILAR process.[32] As shown in Figure 4d and 4e, the presence of CdS QDs can be determined via indexing the binding energy of Cd $3d_{3/2}$ (411.9 eV), Cd $3d_{5/2}$ (405.2 eV), S $2p_{3/2}$ (162.6 eV) and S $2p_{1/2}$ (161.5 eV).[50] Besides, as displayed in Figure 4f the presence of Mn^{2+} dopant can also be detected via the deconvolution of the Mn $2p_{1/2}$ and Mn $2p_{3/2}$ peak (651.9 eV and 640.8 eV).[51]

The valence band (VB) edge was extracted from the XPS analysis (Figure S3). It can be seen that the VB edge of pure TNRs is located at 2.92 eV below the Fermi energy, but the VB edge of quaternary CAHT NRs show 0.28 eV VB blue-shifts due to the formation of heterostructures.[11]

To further confirm the existence of Ti^{3+} and Ov in the H-TNRs, A-H-TNRs and CAHT NRs, Electron paramagnetic response (EPR) spectroscopy analysis was also employed (Figure S4). No EPR signals can be detected in pristine TNRs samples. On the other hand, the H-TNRs sample displays two strong signals at $g = 2.005$ and 2.000 corresponding to Ov and Ti^{3+},[41] suggesting that hydrogenation treatment could induce Ov and Ti^{3+} into the TNRs. Furthermore, the EPR signals of A-H-TNRs and CAHT NRs reduced gradually because the additional layer (such as QDs) hinder the collection of EPR signals. Based on these comprehensive characterizations (XRD, Raman, SEM, TEM, XPS and EPR), the formation of multi-dimensional quaternary CAHT NRs hybrid structure with the 3D nanotree morphology can be determined.

The UV-visible diffuse reflectance spectra (DRS) of the TNRs, H-TNRs, A-H-TNRs and CAHT NRs composite are shown in Figure S5a. It can be seen that the introduction of Mn-CdS QDs extends the absorption edge to near 445 nm, which equals an optical bandgap of 2.79 eV. Photoluminescence (PL) spectroscopy is helpful to investigate the surface states, bandgap trap, and electron transfer states in photoresponse materials.[52] Figure S5b shows the PL spectra of TNRs, H-TNRs, A-H-TNRs and quaternary CAHT NRs films excited by a 330 nm laser. The lowest PL is obtained from the quaternary CAHT NRs composites. The band-edge energy level difference between Mn-CdS QDs, anatase TiO_2, hydrogenated TiO_2 and rutile TiO_2 allows the rapid consumption of electron along with the cascading bandgap arrangement.[53] The 3D nanotree morphology can improve the rapid immigration of photocarriers from Mn-CdS QDs into the hierarchical structure, leading to the low PL signals in the composite.[54]

PCP performances

The PEC characterizations helped to assess the PCP efficiency of the as-prepared composites. The photoelectrode was placed in sulfide solution in a salt bridge separated compartment (Figure S12). A 300 W xenon lamp serves as the light source, which is usually employed to provide simulating solar illumination.[55, 56] Figure 5a compares photogenerated currents for TNRs, H-TNRs, A-H-TNRs, and CAHT NRs films. After turning on the light source, the photocurrents of the films are positive, demonstrated the fact that the charges migrate from the composite films to the connected steel.[57] Note that there is a photovoltage between steel and photoelectrode under light excitation, therefore, all measurements for the steel actually reflect the mixed potential of both surfaces, which means a shift in mixed potential forms between photoelectrode and steel surface. When the light was not provided, the photocurrent of all films dropped due to the immediate recombination of e^-/h^+ pairs.[58] The photocurrent values show the following pattern: CAHT NRs (4.8 $mA \cdot cm^{-2}$) > A-H-TNRs (2.7 $mA \cdot cm^{-2}$) > H-TNRs (1.6 $mA \cdot cm^{-2}$) > TNRs (0.4 $mA \cdot cm^{-2}$). The photocurrent density of quaternary CAHT NRs film is higher than those of the other films. Previous works suggested that Mn-CdS QDs were photoexcited to generate more charge carriers in the visible-light region.[59] Meanwhile, the formation of heterojunction with cascaded band alignment facilitates e^-/h^+ pairs depletion.[31]

To estimate the PCP efficiency for 304SS, the films (TNRs, H-TNRs, A-H-TNRs, and quaternary CAHT NRs hybrid composites) were used as photoelectrodes, respectively. The protection performance is investigated by comparing the surface potential changes of 304SS under simulated solar light irradiation.[60] As displayed in Figure 5b, the OCP (open-circuit potential) values of 304SS in 3.5 wt% NaCl solution were investigated. Before being coupled with photoanodes, the 304SS corrosion potential is approximately -0.16 V vs. Ag/AgCl. When this steel is coupled with the photoanodes in the darkness, all surface potential values are more negative than the self-corrosion potential of the 304SS owing to the galvanic effect.[61] After providing the solar light illumination, OCPs rapidly drop to lower values, which could be attributed to the cathodic polarization of 304SS due to the immigration of photogenerated charges from the composite films to the protected steel.[16] The OCPs remains relatively constant resulting from the building equilibrium. The ranking of the OCP values of surface potential is in a sequence as: CAHT NRs (-1.00 V vs. Ag/AgCl) < A-H-TNRs (-0.85 V vs. Ag/AgCl) < H-TNRs (-0.76 V vs. Ag/AgCl) < TNRs (-0.54 V vs. Ag/AgCl). The more negative the OCP value of the connected metal is, the better its anticorrosion efficiency would be.[62] Considering the series of photocurrent strength, it is clear that the CAHT NRs film with 3D nanotree morphology perform the best anticorrosion efficiency for the steel.

As displayed in Figure 5b, when Mn-CdS QDs as “fruit” grown on the branch surfaces to form 3D nanotree morphology, the PCP performance of as-prepared quaternary CAHT NRs hybrid composite is much better than ternary and binary systems. The narrow bandgap of Mn-CdS QDs and the formation of stepwise bandgap steps are the main reason for the superior PCP performance. The multi-dimensional shortcut of A-H-TNRs substrate also accelerates the electronic migration from photoanode to 304SS.[53] As shown in Figure 5c and 5d, the photoresponse could be ranked as follows: CAHT NRs (4.8 mA·cm^{-2}) > Mn-CdS QDs/Anatase TiO_2 branches/TNRs (CMS-A-TNRs, 4.3 mA·cm^{-2}) > Mn-CdS QDs/Hydrogenated-TiO_2 layer/TNRs (CMS-H-TNRs, 3.2 mA·cm^{-2}) > Anatase TiO_2 branches/Hydrogenated-TiO_2 layer/TNRs (A-H-TNRs, 2.7 mA·cm^{-2}). The sequence of surface potential can be ranked as follow: CAHT NRs (-1.00 V vs. Ag/AgCl) < CMS-A-TNRs (-0.96 V vs. Ag/AgCl) < CMS-H-TNRs (-0.93 V vs. Ag/AgCl) < A-H-TNRs (-0.85 V vs. Ag/AgCl).

The comparison of full scan survey XPS spectra between CAHT NRs and CMS-H-TNRs samples are displayed in Figure 5e to investigate the content variation of Mn-CdS QDs on the sample surfaces. The atomic percentage of Cd corresponds to the CAHT NRs (15.82%), and CMS-H-TNRs (4.42%) indicates that the CAHT NRs nanotree can host more Mn-CdS QDs to improve PCP performances. The OCPs of 304SS connected with CAHT NRs composite with 3D nanotree morphology remain negative (-0.5 V vs. Ag/AgCl at 1400 s) of the initial potential (-0.31 V vs. Ag/AgCl at 0 s) even after turning off the light source, which implies that the time-delay protection effect is possible.[38]

In addition to 304SS, 65Mn carbon steel (65Mn CS), as a representative carbon steel, was also coupled to photoanodes with these films to investigate their PCP efficiency. The OCP values of the 65Mn CS, connected to the unmodified TNRs (-0.77 V vs. Ag/AgCl) or CAHT NRs (-1.02 V vs. Ag/AgCl) (Figure S6a) dropped below its self-corrosion potential (65Mn CS, -0.57 V vs. Ag/AgCl, as shown in Figure S6b), implying that the CAHT NRs composite could have the ability to protect carbon steel. As shown in Table S1, compared with previously reported binary and ternary photoanodes for PCP, the quaternary CAHT NRs hybrid composite superstructure displayed the excellent anticorrosion performance.

Tafel curves of uncoupled 304SS and 304SS coupled with as-prepared photoelectrodes were measured with and without solar light illumination to further analyze the PCP mechanism. As shown in Figure 5f, the corrosion potential (E_{corr}) of 304SS connected with these composites displays an offset value from -0.54 to -0.97 V vs. Ag/AgCl compared with that of uncoupled 304SS (-0.16 V vs. Ag/AgCl) under solar irradiation. The E_{corr} of 304SS, coupled with CAHT NRs composite, displays the lowest value (-0.97 V vs. Ag/AgCl), and this result agrees with the above OCP discussion. It is known that the high corrosion current density (j_{corr}) value could improve anti-corrosion efficiency under solar irradiation.[63] According to the Tafel test results, the j_{corr} of CAHT NRs/304SS (128.82 $\mu A \cdot cm^{-2}$) is clearly higher than that of the remaining samples/304SS (24.55 $\mu A \cdot cm^{-2}$ to 57.54 $\mu A \cdot cm^{-2}$) and uncoupled 304SS (2.24 $\mu A \cdot cm^{-2}$). In contrast with uncoupled 304SS, the dark E_{corr} of the 304SS (Figure S7) changes to a more positive value after being connected with as-prepared photoanodes (to -0.11 V with TNRs, -0.06 V with H-TNRs, 0.01 V with A-H-TNRs, 0.07 V with CAHT NRs, vs. Ag/AgCl). The j_{corr} values of the 304SS coupled with the TNRs, H-TNRs, A-H-TNRs and CAHT NRs photoanodes are 0.89, 0.37, 0.24 and 0.20 $\mu A \cdot cm^{-2}$, respectively, and these values are more negative than that of the unconnected 304SS in darkness. The

j_{corr} value in darkness is positively associated with the self-corrosion rate of the metal.[16] These tests indicate that some protection for 304SS persists even in darkness.

The stability and time-delay protection evaluation of quaternary CAHT NRs hybrid composite films

To investigate the photogenerated potential stability of quaternary CAHT NRs hybrid composite film in PCP, surface potential variations as a function of light intermission were investigated (as shown in Figure 6a). The OCP value (around -0.87 V vs. Ag/AgCl) of 304SS is still lower than its initial value (around -0.28 V vs. Ag/AgCl) after intermittent eight hours' solar light illumination. The stability of crystalline structure of the CAHT NRs has been examined after the PCP experiment. In Figure 6b, SEM analysis confirmed that the radiating anatase branches still cover the surface of the nanorod. Due to Mn-CdS QDs playing an essential role in enhancing the PCP performance of the whole composite, we carried out EDS and XPS analysis before and after the PCP test to probe the content varition. The EDS spectrum (Figure S8) reveals Cd, S and Mn elements after PCP analysis. As shown in Figure 6c, the full scan survey XPS spectrum demonstrates that the Cd and Mn element content just declines from 15.82% to 13.06% and from 2.78% to 2.64%, respectively. Only a small amount of QDs have been lost from the surface after PCP analysis. The XRD result of the CAHT NRs film before and after the PCP test (Figure S9) further confirms a negligible peak location and relative peak intensity variation.

As shown in Figure 6d, the dark time-delay effect of quaternary CAHT NRs hybrid composite for avoiding the corrosion of 304SS is estimated under long-period intermittently solar light illumination. After switching off the light source (1 h solar light illumination), the surface potential of the 304SS shift to -0.34 V vs. Ag/AgCl immediately. Then, the OCPs value of 304SS, connected with the CAHT NRs film, returned slowly to the start state, indicating that the CAHT NRs film can offer continuous protection (~3.78 h) even after cutting off the light. These types of effects are obviously dependent on electrode sizes and conditions in the electrolyte.

Electrochemical impedance spectroscopy (EIS) has been broadly used to study the photocarrier-transfer mechanism of photoanode owing to the sensitivity and non-destructive natures.[64] Figure 6e displays the Nyquist plots of the as-prepared films (TNRs, H-TNRs, A-H-TNRs and CAHT NRs films) under solar light illumination. Both the TNRs and H-TNRs have a big and incomplete semicircle. However, for A-H-TNRs and CAHT NRs, two small and incomplete semicircles are located in the high-frequency and low-frequency regions. The Bode plots in Figure 6f show that TNRs and H-TNRs have two peaks, whereas the others have three peaks, which could be assigned to the microstructure differences.[65] Therefore, TNRs and H-TNRs with 1D nanorod morphology have two-time-constant, and A-H-TNRs and CAHT NRs films with 3D anatase branches have three-time-constants. Models of equivalent circuits for EIS results are displayed in Figure 6g. It can be seen that the CAHT NRs film displays the lowest R_{ct} value (0.19 kΩ·cm^2) compared with others (8.27 - 42.38 kΩ·cm^2) (Table S2).

Additionally, this quaternary composite also had the smallest $|Z|_{0.01Hz}$, as displayed in Figure 6f. The smallest R_{ct} and $|Z|_{0.01Hz}$ of the quaternary CAHT NRs film indicate the superior separation and transfer efficiency of interfacial e^-/h^+ pairs.[66] These charges could transfer rapidly to the coupled 304SS leading to an enhanced high PCP performance. In addition, quaternary CAHT NRs hybrid composite can serve as a supercapacitor,[67] which could release the stored electron to coupled 304SS to realize the time-delay protection when turning off the light source.

DFT theoretical simulation

As displayed in Figure 7, the first-principle DFT simulations were carried out to investigate the total and partial density of states (TDOS and PDOS) from samples in this work. For the TNRs (Figure 7a), it's clear that O 2p state electrons are the main constituent of the valance band maximum (VBM) with a small portion from Ti 3d state electrons.[68] However, the conduction band minimum (CBM) is dominated by Ti 3d state electrons and include a tiny number of O 2p state electrons. Hence, the bandgap of TNRs can be confirmed by the energy difference between VBM and CBM. Nevertheless, the experimental value (ca. 3.07 eV) is still higher than this estimated value owing to the commonly underestimated Hubbard interaction by the GGA theoretical calculation approach.[69]

According to the XPS Ti 3d results of H-TNRs, after removing one-twelfth oxygen atoms in the upper three atomic layers (inducing Ov and Ti^{3+}) of the rutile TiO_2-(1 1 0) surface, the Fermi level shifts toward the edge of CB level. As shown in Figure 7b, this change can enhance conductivity,[70] which agree with the EIS results of H-TNRs. Meanwhile, in the green rectangles, the edge of the CB level displays several peaks near the VB, implying the successful introduction of defect levels in the bandgap caused by Ov and Ti^{3+}.[71] Therefore, the shallow donor level can directly promote the local electrons to CBM. As a result, the bandgap of H-TNRs is reduced to be 1.05 eV after hydrogenated treatment, agreeing with the results displayed in the DRS test. Furthermore, the bandgap has been decreased further by growing anatase branches on the surface of the disordered-TiO_2 layer, as shown in Figure 7c.

As shown in Figure 7d, the CAHT NRs composite shows a smaller bandgap (0.36 eV) than A-H-TNRs samples, which is also consistent with DRS analysis. It has been reported that there will be a strong electronic coupling between adsorbate states (Mn-CdS QDs) and the substrate state (i.e. A-H-TNRs),[72] which will lead to the migration of VBM to high energy to reduce the bandgap of A-H-TNRs. Meanwhile, the electronic hybridization can be enhanced among Ti 3d, O 2p, Cd 4d, S 3p and Mn 3d states. A high-level extent of hybridization in the VB and CB levels is beneficial to the electrocatalytic process because it could enhance the transfer of electrons [73]. The VBM is dominated by the S 3p state (e.g. CdS), but the CBM is defined by Ti 3d (Figure S10). Therefore, the photoexcited electron could easily transfer from the S 3p state to Ti 3d state under illumination. The doping energy level (Mn 3d state) promotes the hybridization of the density of states [74] and serve as a defect state to capture the photocarriers for enhancing PCP performances.

Mechanism

Mott-Schottky curve test was carried out to study the PCP mechanism.[75] As displayed in Figure S11a, all as-prepared composite display positive slopes of the Mott-Schottky plot, implying the n-type semiconductor natures.[76] According to the previous studies,[77] the slope value of the Mott-Schottky plot is negatively correlated with the carrier concentration. The slope value of the curve of CAHT NRs film is the most negative among all the as-prepared films, confirming the high-level free carrier amount. The flat band (FB) potential of a semiconductor can be estimated by the linear parts of the curves extrapolating the plots to $Cs^{-2} = 0$,[78] which is -0.16, -0.22, -0.36, and -0.53 V vs. Ag/AgCl (equal to 0.04, -0.02, -0.16 and -0.33 eV vs. normal hydrogen electrode (NHE), respectively) for TNRs, H-TNRs, A-H-TNRs and CAHT NRs respectively. For n-type semiconductors, because the FB potential represents the strength of the depletion layer formed between the semiconductor surface and the electrolyte, the more cathodic the n-type electrode is, the more efficient the depletion of photogenerated e^-/h^+ pairs would be.[3] Therefore, the CAHT NRs composite exhibits the best PCP performance due to its most cathodic FB value among the as-prepared films.

At equilibrium state, the space charge layer in CAHT NRs composite film will change due the band edge bending which pushes the Fermi level to align across the interface between semiconductor, electrolyte and the coupled metal (i.e. 304SS).[75] Hence, the Schottky barrier will form between metal/semiconductor interfaces, hindering the electron backflow from protected metal to coupled semiconductor electrodes. For n-type semiconductors, the CBM energy level of an n-type semiconductor is about -0.1 or - 0.2 eV negative than its FB potential.[79] Therefore, at open circuit condition, the band edge levels and band alignments between TNRs, H-TNRs, A-H-TNRs and CAHT NRs can be estimated. As shown in Figure S11b, the quaternary CAHT NRs composite possesses the most negative CB level (-0.53 eV vs. NHE), so the Schottky barrier between CAHT NRs/304SS interface is higher than that of the others. Meanwhile, the remarkable negative shift of the CB level indicates that the electrons located at CB level have strongest driving force to transmit to the coupled 304SS,[80] which also underpins the superior PCP performance as demonstrated earlier.

The unique morphology of the 3D nanotree-like structure (Scheme 2) for enhancing PCP efficiency can be rationalized as follows: i), the rutile-TiO_2 nanorod as the trunk of nanotree structure can sustain radial depletion layers, which can significantly enhance spatial separation of photogenerated carriers. ii), the hydrogenated-TiO_2 layer as the bark of nanotree could provide Ov and Ti^{3+} as defect level as sub-bandgap, which expand the absorption edge. iii), the radiating anatase-TiO_2 branches could enlarge the photon-harvesting surface area and provide more depositing sites for accommodating QDs. iv), the Mn-CdS QDs with narrow bandgap can enrich the visible-light absorption and further strength the PCP efficiency. v), when switching off the light source, the momentarily reserved charges in the composite could be unleashed and immigrated to the connected steel, indicating the time-delay cathodic protection for the steel even in darkness.[38] This effect is linked to the presence of the sulfide electrolyte in the experiments reported here, but could be possible also for photoanodes in seawater. Future work will address the development of photoanodes that operate without the need for a sacrificial electrolyte.

Conclusion

In summary, a unique quaternary CAHT NRs superstructure has been proposed as a PCP photoanode towards energy level cascaded “quantum armours” combating metal corrosion. A two-step hydrothermal method, hydrogenation treatment, and the SILAR deposition process were employed to successfully grow this quaternary structure. We demonstrate cathodic protection could be realized under simulated solar light irradiation as well as persistent time-delay protection. Although complex, the new growth methodology of this quaternary composite superstructure, together with nanotree morphology, could provide a generic approach for designing the high-efficiency PEC systems beyond PCP, in solar fuels, artificial photosynthesis, and in water splitting. Currently, the photo-protection process is linked to the presence of sulfide in solution which is a sacrificial component of the system. In the future, improvement in the process will be necessary to overcome the reliance on sacrificial components towards real seawater/brine PCP applications.

Experimental

The thorough details of chemicals, experimental devices, and DFT computation approach were introduced in the Supporting Materials (SM).

Synthesis method

Preparation of TNRs film: TNRs array film was synthesized through the hydrothermal reaction according to our previous report [7].

Preparation of hydrogenated TNRs (H-TNRs) film: The as-prepared TNRs array was calcined again in a quartz tube furnace under 10% H_2/Ar atmosphere at 450 °C for 2 h with a heating/cooling rate of 5 $°C \cdot min^{-1}$.

Preparation of anatase TiO_2 branch/HTNRs (A-H-TNRs) film: Firstly, HTNRs film was vertically immersed in a 0.5 $mol \cdot L^{-1}$ $TiCl_4$ aqueous solution under ambient conditions for 1 h, then placed in a Teflon-lined stainless-steel autoclave at 180 °C. The treated film was leaned at 60 degrees against the autoclave wall in a solution, with the conductive side facing down. The solution contained 35 mL distilled water (DIW), 0.5 mL H_2SO_4 (98 wt%), and 0.2 mL $C_{16}H_{36}O_4Ti$. After secondary hydrothermal reaction for 3 h, the sample was washed with DIW until the pH value of cleaning fluid remain around 7. Finally, those composites were calcined at 400 °C for 2 h in the air.

Preparation of CAHT NRs film: The Mn-CdS QDs were deposited on the A-HTNRs by the SILAR method [32]. For each SILAR cycle, the sample was dipped into the methanolic solutions of 0.04 M $Cd(CH_3COO)_2$ and 0.01 M $Mn(CH_3COO)_2$ (Mn/(Mn + Cd) molar ratios = 20%) for 5 min, and then immersed into 0.05 $mol \cdot L^{-1}$ $Na_2S \cdot 9H_2O$ in methanol plus water (1:1, V/V) for another 5 min. Following each immersion, the as-prepared samples were rinsed with methanol and DIW in succession and then dried at room temperature. The Mn-CdS QDs deposition was performed through 5 cycles of the SILAR process. Finally, the composite films were calcined in a muffle furnace at 300 °C for 2 h in the air.

PEC tests

The photocurrent density, open-circuit potential (OCP) and Tafel experiments were carried out on the CHI660E electrochemical workstation (Shanghai Chinstrument Co. Ltd, China) using a double electrolytic cell setup, composed of a corrosion cell (3.5 wt% NaCl solution), a PEC cell (0.1 M Na_2S and 0.2 M NaOH mixed solution) and two couple cells coupled by a salt bridge (a U-type glass tube filled with 1.0 M KCl in agar) (Figure S12). In the corrosion cell, a three-electrode configuration was used, which contains stainless steel, Ag/AgCl electrode and Pt foil as the working electrode (WE), reference electrode (RE) and counter electrode (CE), respectively. The as-prepared CAHT NRs film was immersed in the PEC cell as the photoanode and connected with the protected steel by a copper wire. PEC measurements were conducted under intermittent simulated sunlight with a 300 W xenon lamp (PLS-SXE300/300UV, Beijing Bofeilai Co., Beijing, China). Photocurrent curves and OCP curves were carried out at a 0 V (vs. Ag/AgCl) bias potential with intermittent light on/off. The Tafel curves were tested in a potential range of -1 - 1 V vs. Ag/AgCl with 0.01 V/s scan rate

The electrochemical impedance spectroscopy (EIS) and Mott-Schottky (MS) plots were measured on the photoanode in a conventional photoelectrochemical three-electrode cell (0.5 M Na_2SO_4 solution) using CHI660E electrochemical workstation. A three-electrode configuration was used, which contains photoanode, saturated calomel electrode and Pt foil as the WE, RE and CE, respectively. The EIS was tested at the photoinduced potential over a frequency range of 10^5 to 10^{-2} Hz with a 10 mV AC amplitude. Mott-Schottky plots were then conducted at the frequency of 1000 Hz by 10 mV alternating current amplitude. The active area of 304SS and 65Mn carbon steel (65Mn CS) and as-prepared CAHT NRs film were 1 cm^2, and the 304SS and 65Mn CS were polished with abrasive paper before each test.

Acknowledgements

This work was supported by the National Natural Science Foundation of China (Grant No. 21507104).

Reference

[1] X. Wang, H. Xu, Y. Nan, X. Sun, J. Duan, Y. Huang, B. Hou, Research progress of TiO_2 photocathodic protection to metals in marine environment, J Oceanol Limnol 38 (2020) 1018.

[2] A. Konoplev, V. Kanivets, O. Zhukova, M. Germenchuk, H. Derkach, Mid- to long-term radiocesium wash-off from contaminated catchments at Chernobyl and Fukushima, Water Res. 188 (2021) 116514.

[3] S. Guo, L. Chi, T. Zhao, Y. Nan, X. Sun, Y. Huang, B. Hou, X. Wang, Construction of MOF/TiO_2 nanocomposites with efficient visible-light-driven photocathodic protection, J. Electroanal. Chem. 880 (2021) 114915.

[4] M.R. Ortíz, M.A. Rodríguez, R.M. Carranza, Effect of crevice corrosion inhibitors on the passivity of alloy 22, J. Electrochem. Soc. 159 (2012) C469-C475.

[5] H.D. Johansen, C.M.A. Brett, A.J. Motheo, Corrosion protection of aluminium alloy by cerium conversion and conducting polymer duplex coatings, Corros. Sci. 63 (2012) 342-350.

[6] P. Refait, M. Jeannin, R. Sabot, H. Antony, S. Pineau, Corrosion and cathodic protection of carbon steel in the tidal zone: Products, mechanisms and kinetics, Corros. Sci. 90 (2015) 375-382.

[7] Y. Liu, C. Zhao, X. Wang, H. Xu, H. Wang, X. Zhao, J. Feng, W. Yan, Z. Ren, Preparation of PPy/TiO_2 core-shell nanorods film and its photocathodic protection for 304 stainless steel under visible light, Mater. Res. Bull. 124 (2020) 110751.

[8] H. Xu, W. Liu, L. Cao, G. Su, R. Duan, Preparation of porous TiO_2/ZnO composite film and its

photocathodic protection properties for 304 stainless steel, Appl. Surf. Sci. 301 (2014) 508-514.

[9] Y. Wang, J. Yu, W. Xiao, Q. Li, Microwave-assisted hydrothermal synthesis of graphene based Au-TiO_2 photocatalysts for efficient visible-light hydrogen production, J. Mater. Chem. A 2 (2014) 3847-3855.

[10] J. Hu, Z.C. Guan, Y. Liang, J.Z. Zhou, Q. Liu, H.P. Wang, H. Zhang, R.G. Du, Bi_2S_3 modified single crystalline rutile TiO_2 nanorod array films for photoelectrochemical cathodic protection, Corros. Sci. 125 (2017) 59-67.

[11] N. Wei, Y. Liu, M. Feng, Z. Li, S. Chen, Y. Zheng, D. Wang, Controllable TiO_2 core-shell phase heterojunction for efficient photoelectrochemical water splitting under solar light, Appl. Catal., B 244 (2019) 519-528.

[12] M. Motola, L. Satrapinskyy, M. Čaplovicová, T. Roch, M. Gregor, B. Grančič, J. Greguš, Ľ. Čaplovič, G. Plesch, Enhanced photocatalytic activity of hydrogenated and vanadium doped TiO_2 nanotube arrays grown by anodization of sputtered Ti layers, Appl. Surf. Sci. 434 (2018) 1257-1265.

[13] B. Liu, J. Wang, J. Yang, X. Zhao, Charge carrier interfacial transfer pathways from TiO_2 and Au/TiO_2 nanorod arrays to electrolyte and the association with photocatalysis, Appl. Surf. Sci. 464 (2019) 367-375.

[14] Z. Liang, H. Hou, Z. Fang, F. Gao, L. Wang, D. Chen, W. Yang, Hydrogenated TiO_2 nanorod arrays decorated with carbon quantum dots toward efficient photoelectrochemical water splitting, ACS Appl. Mater. Interfaces 11 (2019) 19167-19175.

[15] M. Feng, Y. Liu, S. Zhang, Y. Liu, N. Luo, D. Wang, Carbon quantum dots (CQDs) modified TiO_2 nanorods photoelectrode for enhanced photocathodic protection of Q235 carbon steel, Corros. Sci. 176 (2020) 108919.

[16] W. Sun, N. Wei, H. Cui, Y. Lin, X. Wang, J. Tian, J. Li, J. Wen, 3D $ZnIn_2S_4$ nanosheet/TiO_2 nanowire arrays and their efficient photocathodic protection for 304 stainless steel, Appl. Surf. Sci. 434 (2018) 1030-1039.

[17] J. Zhang, R.G. Du, Z.Q. Lin, Y.F. Zhu, Y. Guo, H.Q. Qi, L. Xu, C.J. Lin, Highly efficient CdSe/CdS co-sensitized TiO_2 nanotube films for photocathodic protection of stainless steel, Electrochim. Acta 83 (2012) 59-64

[18] J. Li, C.J. Lin, J.T. Li, Z.Q. Lin, A photoelectrochemical study of CdS modified TiO_2 nanotube arrays as photoanodes for cathodic protection of stainless steel, Thin Solid Films 519 (2011) 5494-5502.

[19] Y.L. Chen, Y.H. Chen, J.W. Chen, F. Cao, L. Li, Z.M. Luo, I.C. Leu, Y.C. Pu, New insights into the electron collection efficiency improvement of CdS-sensitized TiO_2 nanorod photoelectrodes by interfacial seed-layer mediation, ACS Appl. Mater. Interfaces 11 (2019) 8126.

[20] G.P. Kissling, D. Fermín, Electrochemical hole injection into the valence band of thiol stabilised CdTe quantum dots, Phys. Chem. Chem. Phys. 11 (2009) 10080-10086.

[21] Z. Li, X. Wang, X. Wang, Y. Lin, A. Meng, L. Yang, Q. Li, Mn-Cd-S@amorphous-Ni_3S_2 hybrid catalyst with enhanced photocatalytic property for hydrogen production and electrocatalytic OER, Appl. Surf. Sci. 491 (2019) 799-806.

[22] L. Yu, L. Zhen, Y. Liu, F. Cheng, S. Sun, Mn-doped CdS quantum dots sensitized hierarchical TiO_2 flower-rod for solar cell application, Appl. Surf. Sci. 305 (2014) 359-365.

[23] Y. Wang, S. Ge, L. Zhang, J. Yu, M. Yan, J. Huang, Visible photoelectrochemical sensing platform by in situ generated CdS quantum dots decorated branched-TiO_2 nanorods equipped with Prussian blue electrochromic display, Biosens. Bioelectron. 89 (2016) 859-865.

[24] A. Qileng, Y. Cai, J. Wei, H. Lei, W. Liu, S. Zhang, Y. Liu, Construction of CdS/B-TiO_2 nanorods

photoelectrochemical immunosensor for the detection of microcystin-LR using SiO_2@G-quadruplex as multi-amplifier, Sens. Actuators, B 254 (2018) 727.

[25] X. Yu, Z. Zhao, J. Zhang, W. Guo, J. Qiu, D. Li, Z. Li, X. Mou, L. Li, A. Li, H. Liu, Rutile nanorod/anatase nanowire junction array as both sensor and power supplier for high-performance, self-powered, wireless UV photodetector, Small 12(20) (2016) 2759-67.

[26] C. Gao, T. Wei, Y. Zhang, X. Song, Y. Huan, H. Liu, M. Zhao, J. Yu, X. Chen, A photoresponsive rutile TiO_2 heterojunction with enhanced electron-hole separation for high-performance hydrogen evolution, Adv Mater 31 (2019) e1806596.

[27] A. Mahmood, G. Shi, Z. Wang, Z. Rao, W. Xiao, X. Xie, J. Sun, Carbon quantum dots-TiO_2 nanocomposite as an efficient photocatalyst for the photodegradation of aromatic ring-containing mixed VOCs: An experimental and DFT studies of adsorption and electronic structure of the interface, J Hazard Mater 401 (2021) 123402.

[28] X. Wang, S. Zhang, Y. Xie, H. Wang, H. Yu, Y. Shen, Z. Li, S. Zhang, F. Peng, Branched hydrogenated TiO_2 nanorod arrays for improving photocatalytic hydrogen evolution performance under simulated solar light, Int. J. Hydrogen Energy 41 (2016) 20192-20197.

[29] R. Wang, M. Zu, S. Yang, S. Zhang, W. Zhou, Z. Mai, C. Ge, Y. Xu, Y. Fang, S. Zhang, Visible-light-driven photoelectrochemical determination of Cu^{2+} based on CdS sensitized hydrogenated TiO_2 nanorod arrays, Sens. Actuators, B 270 (2018) 270-276.

[30] H. Wei, W.A. McMaster, J.Z.Y. Tan, D. Chen, R.A. Caruso, Tricomponent brookite/anatase TiO_2/g-C_3N_4 heterojunction in mesoporous hollow microspheres for enhanced visible-light photocatalysis, J. Mater. Chem. A 6 (2018) 7236-7245.

[31] Z.C. Guan, X. Wang, P. Jin, Y.Y. Tang, H.P. Wang, G.L. Song, R.G. Du, Enhanced photoelectrochemical performances of ZnS-Bi_2S_3/TiO_2/WO_3 composite film for photocathodic protection, Corros. Sci. 143 (2018) 31-38.

[32] A. Xl, A. Ch, S.A. Jin, A. Hls, B. Flyl, C. Wyta, Enhanced photoelectrochemical charge transfer on Mn-doped CdS/TiO_2 nanotube arrays: The roles of organic substrates, Catal. Today 335 (2019) 468-476.

[33] B. Hou, D. Parker, G.P. Kissling, J.A. Jones, D. Cherns, D.J. Fermín, Structure and band edge energy of highly luminescent $CdSe_{1-x}Te_x$ alloyed quantum dots, J. Phys. Chem. C 117 (2013) 6814-6820.

[34] P. Soundarrajan, K. Sankarasubramanian, T. Logu, K. Sethuraman, K. Ramamurthi, Growth of rutile TiO_2 nanorods on TiO_2 seed layer prepared using facile low cost chemical methods, Mater. Lett. 116 (2014) 191-194.

[35] X. Xu, J. Cai, M. Zhou, X. Du, Y. Zhang, Photoelectrochemical degradation of 2,4-dichlorophenoxyacetic acid using electrochemically self-doped Blue TiO_2 nanotube arrays with formic acid as electrolyte, J Hazard Mater 382 (2020) 121096.

[36] A.R. Zanatta, A fast-reliable methodology to estimate the concentration of rutile or anatase phases of TiO_2, AIP Adv. 7 (2017) 075251.

[37] S. Kumar, A.K. Ojha, In-situ synthesis of reduced graphene oxide decorated with highly dispersed ferromagnetic CdS nanoparticles for enhanced photocatalytic activity under UV irradiation, Mater. Chem. Phys. 171 (2016) 126-136.

[38] Y. Liu, J. Lu, W. Zhang, C. Lin, Z. Wang, X. Wang, H. Xu, J. Feng, B. Hou, W. Yan, Z. Ren, Efficient photocathodic protection enabled by a multi-dimensional quaternary hybrid superstructure, Chem. Eng. J. 421 (2020) 127858.

[39] S.J. Kwon, H.B. Im, J.E. Nam, J.K. Kang, T.S. Hwang, K.B. Yi, Hydrothermal synthesis of rutile–

anatase TiO_2 nanobranched arrays for efficient dye-sensitized solar cells, Appl. Surf. Sci. 320 (2014) 487-493.

[40] K. Hagedorn, C. Forgacs, S. Collins, S. Maldonado, Design considerations for nanowire heterojunctions in solar energy conversion/storage applications, J. Phys. Chem. C 114 (2010) 12010-12017.

[41] J. Song, M. Zheng, X. Yuan, Q. Li, F. Wang, L. Ma, Y. You, S. Liu, P. Liu, D. Jiang, L. Ma, W. Shen, Electrochemically induced Ti^{3+} self-doping of TiO_2 nanotube arrays for improved photoelectrochemical water splitting, J. Mater. Sci. 52 (2017) 6976-6986.

[42] C. Zhu, M. Shi, S. Yang, H. Zhang, Z. Yang, B. Ding, Growth of radial arranged TiO_2 nanorods by direct oxidation of Al-coated In-738 superalloy, J. Alloys Compd. 485(1) (2009) 328-332.

[43] M.A. Mohamed, J. Jaafar, M.F. M. Zain, L.J. Minggu, M.B. Kassim, M.S. Rosmi, N.H. Alias, N.A. Mohamad Nor, W.N. W. Salleh, M.H.D. Othman, In-depth understanding of core-shell nanoarchitecture evolution of g-C_3N_4@C, N co-doped anatase/rutile: Efficient charge separation and enhanced visible-light photocatalytic performance, Appl. Surf. Sci. 436 (2018) 302-318.

[44] Z. Yan, W. Wang, L. Du, J. Zhu, D.L. Phillips, J. Xu, Interpreting the enhanced photoactivities of 0D/1D heterojunctions of CdS quantum dots /TiO_2 nanotube arrays using femtosecond transient absorption spectroscopy, Appl. Catal., B 275 (2020) 119151.

[45] X. Lu, L. Liu, J. Ge, Y. Cui, F. Wang, Morphology controlled synthesis of $Co(OH)_2/TiO_2$ p-n heterojunction photoelectrodes for efficient photocathodic protection of 304 stainless steel, Appl. Surf. Sci. 537 (2021) 148002.

[46] J. Liu, M. Dai, J. Wu, Y. Hu, Q. Zhang, J. Cui, Y. Wang, H.H. Tan, Y. Wu, Electrochemical hydrogenation of mixed-phase TiO_2 nanotube arrays enables remarkably enhanced photoelectrochemical water splitting performance, Sci. Bull. 63 (2018) 194-202.

[47] Y. Yang, W. Zhang, Y. Xu, H. Sun, X. Wang, Ag_2S decorated TiO_2 nanosheets grown on carbon fibers for photoelectrochemical protection of 304 stainless steel, Appl. Surf. Sci. 494 (2019) 841-849.

[48] C. Han, Q. Shao, J. Lei, Y. Zhu, S. Ge, Preparation of NiO/TiO_2 p-n heterojunction composites and its photocathodic protection properties for 304 stainless steel under simulated solar light, J. Alloys Compd. 703 (2017) 530-537.

[49] J. Hu, S. Zhang, Y. Cao, H. Wang, H. Yu, F. Peng, Novel Highly Active Anatase/Rutile TiO_2 Photocatalyst with Hydrogenated Heterophase Interface Structures for Photoelectrochemical Water Splitting into Hydrogen, ACS Sustainable Chem. Eng., 6 (2018) 10823-10832.

[50] J. Chen, Z. Xia, H. Li, Q. Li, Y. Zhang, Preparation of highly capacitive polyaniline/black TiO_2 nanotubes as supercapacitor electrode by hydrogenation and electrochemical deposition, Electrochim. Acta 166 (2015) 174-182.

[51] U. Jabeen, T. Adhikari, D. Pathak, S.M. Shah, J.-M. Nunzi, Structural, optical and photovoltaic properties of P3HT and Mn-doped CdS quantum dots based bulk hetrojunction hybrid layers, Opt. Mater., 78 (2018) 132-141.

[52] M. Meksi, A. Turki, H. Kochkar, L. Bousselmi, C. Guillard, G. Berhault, The role of lanthanum in the enhancement of photocatalytic properties of TiO_2 nanomaterials obtained by calcination of hydrogenotitanate nanotubes, Appl. Catal., B 181 (2016) 651-660.

[53] J. Hu, Y. Li, S. Zhang, Q. Zhang, Y. Liu, J. Zuo, Q. Li, F. Peng, MoS_2 supported on hydrogenated TiO_2 heterostructure film as photocathode for photoelectrochemical hydrogen production, Int. J. Hydrogen Energy 44 (2019) 31008-31019.

[54] W.Q. Wu, B.X. Lei, H.S. Rao, Y.F. Xu, Y.F. Wang, C.Y. Su, D.B. Kuang, Hydrothermal fabrication

of hierarchically anatase TiO_2 nanowire arrays on FTO glass for dye-sensitized solar cells, Sci. Rep. 3 (2013) 1352.

[55] B. Hou, B.S. Kim, H.K.H. Lee, Y. Cho, P. Giraud, M. Liu, J. Zhang, M.L. Davies, J.R. Durrant, W.C. Tsoi, Z. Li, S.D. Dimitrov, J.I. Sohn, S. Cha, J.M. Kim, Multiphoton absorption stimulated metal chalcogenide quantum dot solar cells under ambient and concentrated irradiance, Adv. Funct. Mater. 30 (2020) 2004563.

[56] B. Hou, Y. Cho, B.S. Kim, J. Hong, J.B. Park, S.J. Ahn, J.I. Sohn, S. Cha, J.M. Kim, Highly monodispersed PbS quantum dots for qutstanding cascaded-junction solar cells, ACS Energy Lett. 1 (2016) 834-839.

[57] X. Lu, L. Liu, X. Xie, Y. Cui, F. Wang, Long-term dual cathodic protection for Q235 carbon steel by $Co(OH)_2$/graphene/TiO_2 photocatalytic material and traditional sacrificial anode, J. Electrochem. Soc. 167 (2020) 131509.

[58] X. Wang, Z.C. Guan, P. Jin, Y.Y. Tang, G.L. Song, G.K. Liu, R.G. Du, Facile fabrication of $BiVO_4$ modified TiO_2 nanotube film photoanode and its photocathodic protection effect on stainless steel, Corros. Sci. 157 (2019) 247-255.

[59] A.H. Davis, E. Hofman, K. Chen, Z.J. Li, A. Khammang, H. Zamani, J.M. Franck, M.M. Maye, R.W. Meulenberg, W. Zheng, Exciton energy shifts and tunable dopant emission in manganese doped two-dimensional CdS/ZnS Core/Shell nanoplatelets, Chem. Mater. 31 (2019) 2516.

[60] H. Li, X. Wang, Q. Wei, X. Liu, Z. Qian, B. Hou, Enhanced photocathodic protection performance of Ag/graphene/TiO_2 composite for 304SS under visible light, Nanotechnology 28 (2017) 225701.

[61] J. Shao, Z.D. Zhang, X.T. Wang, X.D. Zhao, X.B. Ning, J. Lei, X.R. Li, B.R. Hou, Synthesis and photocathodic protection properties of nanostructured SnS/TiO_2 composites, J. Electrochem. Soc. 165 (2018) H601-H606.

[62] X. Xie, L. Liu, R. Chen, G. Liu, Y. Li, F. Wang, Long-Term photoelectrochemical cathodic protection by $Co(OH)_2$-modified TiO_2 on 304 stainless steel in marine environment, J. Electrochem. Soc. 165 (2018) H3154-H3163.

[63] L. Fan, X. Zhang, C. Zhang, J. Li, C. Wu, Y. Chu, F. Ge, Y. Liu, X. Xiong, A highly efficient α-Fe_2O_3/$NiFe(OH)_x$ photoelectrode for photocathodic protection of 304 stainless steel under visible light, Surf. Coat. Technol. 403 (2020) 126407.

[64] Y. Yang, Y.F. Cheng, Bi-layered CeO_2/$SrTiO_3$ nanocomposite photoelectrode for energy storage and photocathodic protection, Electrochim. Acta 253 (2017) 134-141.

[65] X. Zhang, G. Chen, W. Li, D. Wu, Graphitic carbon nitride homojunction films for photocathodic protection of 316 stainless steel and Q235 carbon steel, J. Electroanal. Chem. 857 (2020) 113703.

[66] H. Zheng, Y. Liu, Y. Zhou, D. Zhao, D. Wang, L. Yun, D. Zhang, L. Zhang, Improved photocathodic protection performance of g-C_3N_4/rGO/ZnS for 304 stainless steel, J. Phys. Chem. Solids 148 (2021) 109672.

[67] V.S. Saji, Review-photoelectrochemical cathodic protection in the dark: a review of nanocomposite and energy-storing photoanodes, J. Electrochem. Soc. 167 (2020) 121505.

[68] Q. Liu, L. Wang, K. Zhao, W. Yan, M. Liu, D. Wei, L. Xi, J. Zhang, 3D branched rutile TiO_2@ rutile SnO_2 nanorods array heteroarchitectures/carbon cloth with an adjustable band gap to enhance lithium storage reaction kinetics for flexible lithium-ion batteries, Electrochim. Acta 354 (2020).

[69] X. Tong, W. Shen, X. Chen, Enhanced H_2S sensing performance of cobalt doped free-standing TiO_2 nanotube array film and theoretical simulation based on density functional theory, Appl. Surf. Sci. 469 (2019) 414-422.

[70] J. Chen, Y. Fu, F. Sun, Z. Hu, X. Wang, T. Zhang, F. Zhang, X. Wu, H. Chen, G. Cheng, R. Zheng, Oxygen vacancies and phase tuning of self-supported black TiO_{2-X} nanotube arrays for enhanced sodium storage, Chem. Eng. J. 400 (2020) 125784.

[71] Z. Chen, L.H. Xu, Q. Chen, P. Hu, Z. Liu, Q. Yu, T. Zhu, H. Liu, G. Hu, Z. Zhu, Spray-pyrolysis-assisted synthesis of yolk@shell anatase with rich oxygen vacancies for efficient sodium storage, J. Mater. Chem. A 7 (2019) 6740.

[72] C. Dong, X. Li, J. Qi, First-principles investigation on electronic properties of quantum dot-sensitized solar cells based on anatase TiO_2 nanotubes, J. Phys. Chem. C 115 (2011) 20307-20315.

[73] Y.A. Sethi, C.S. Praveen, R.P. Panmand, A. Ambalkar, A.K. Kulkarni, S.W. Gosavi, M.V. Kulkarni, B.B. Kale, Perforated N-doped monoclinic $ZnWO_4$ nanorods for efficient photocatalytic hydrogen generation and RhB degradation under natural sunlight, Catal. Sci. Technol. 8 (2018) 2909-2919.

[74] M. Liu, Y. Du, L. Ma, D. Jing, L. Guo, Manganese doped cadmium sulfide nanocrystal for hydrogen production from water under visible light, Int. J. Hydrogen Energy 37 (2012) 730-736.

[75] Y. Xu, W. Zhang, Y. Yang, W. Pang, Photo-induced corrosion or protection: Determining the charge transfer in the semiconductor-metal heterojunction, J. Alloys Compd. 817 (2020) 152746.

[76] Y. Nan, X. Wang, X. Ning, J. Lei, S. Guo, Y. Huang, J. Duan, Fabrication of Ni_3S_2/TiO_2 photoanode material for 304 stainless steel photocathodic protection under visible light, Surf. Coat. Technol. 377 (2019) 124395.

[77] X. Wang, J. Lei, Q. Shao, X. Li, X. Ning, J. Shao, J. Duan, B. Hou, Preparation of $ZnWO_4/TiO_2$ composite film and its photocathodic protection for 304 stainless steel under visible light, Nanotechnology 30 (2018) 045710.

[78] Y. Xu, W. Zhang, W. Yu, J. Ding, H. Sun, Polythiophene-sensitized TiO_2 nanotube arrays for photo-generated cathodic protection of 304 stainless steel, J. Mater. Sci. 56 (2021) 1-14.

[79] C. Wang, W. Gao, N. Liu, Y. Xin, B. Hou, Covalent Organic Framework Decorated TiO_2 Nanotube Arrays for Photoelectrochemical Cathodic Protection of Steel, Corros. Sci., 176 (2020) 108920

[80] X. Yu, S. Wang, X. Zhang, A. Qi, X. Qiao, Z. Liu, M. Wu, L. Li, Z.L. Wang, Heterostructured nanorod array with piezophototronic and plasmonic effect for photodynamic bacteria killing and wound healing, Nano Energy, 46 (2018) 29-38.

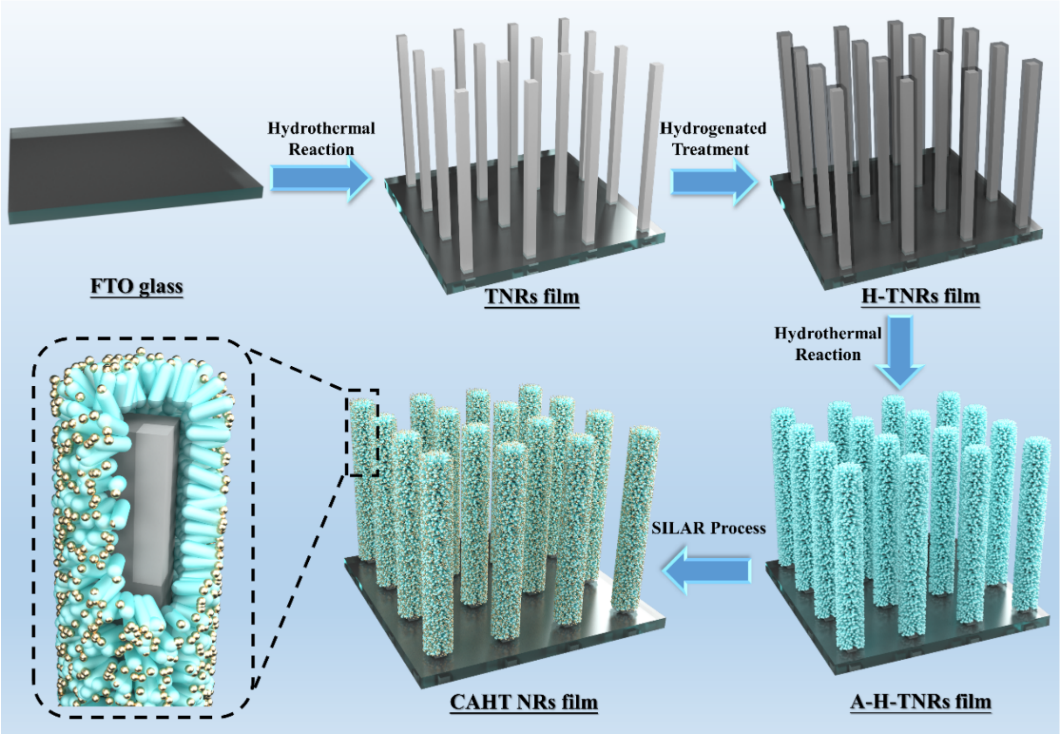

Scheme 1. Schematic illustration of the synthesis process for the quaternary CAHT NRs hybrid composite film.

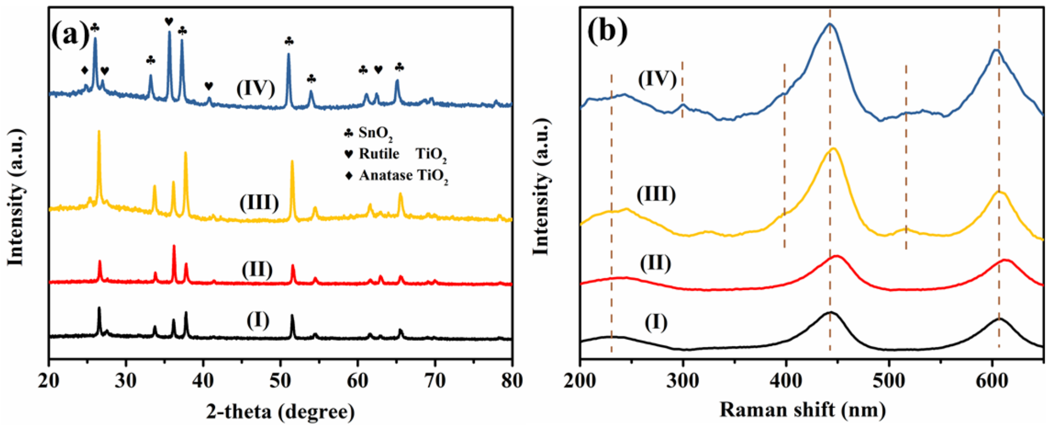

Figure 1. The XRD spectra (a) and the Raman patterns (b) of TNRs (I), H-TNRs (II), A-H-TNRs (III) and hybrid CAHT NRs (IV).

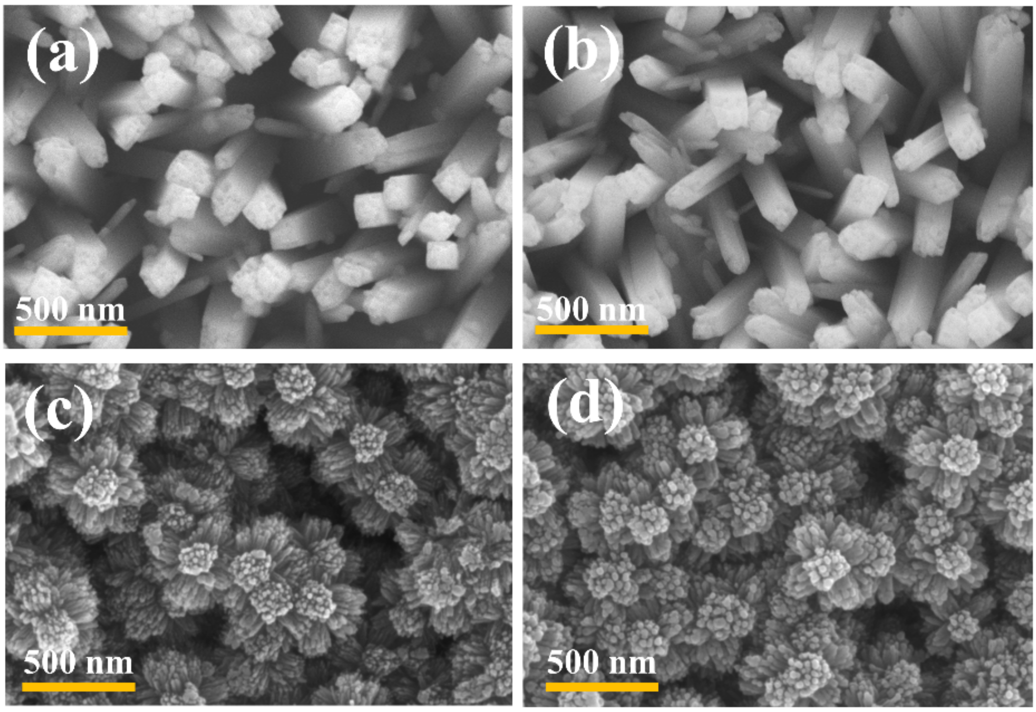

Figure 2. Top-view SEM images of the TNRs (a), H-TNRs (b), A-H-TNRs (c) and CAHT NRs (d) composite films.

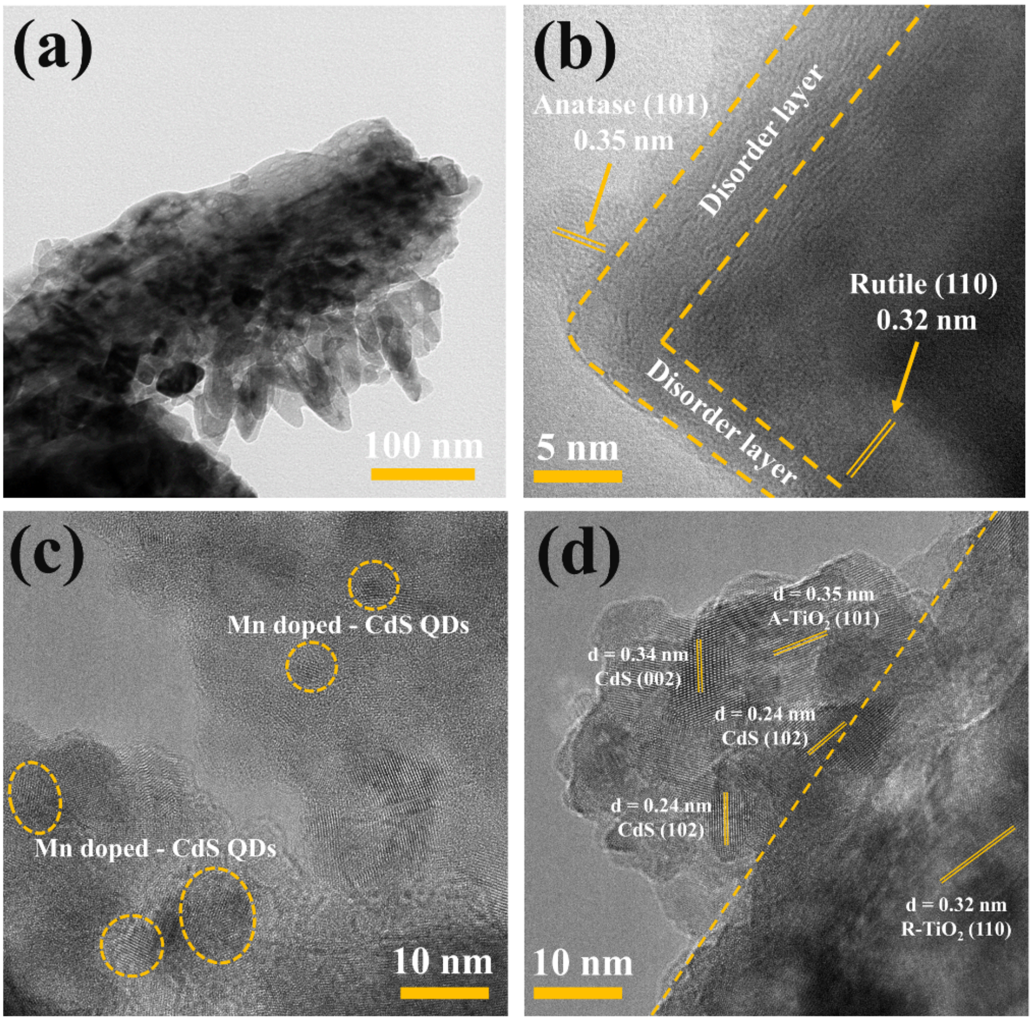

Figure 3. TEM image (a) and HRTEM images (b-d) of CAHT NRs composite films.

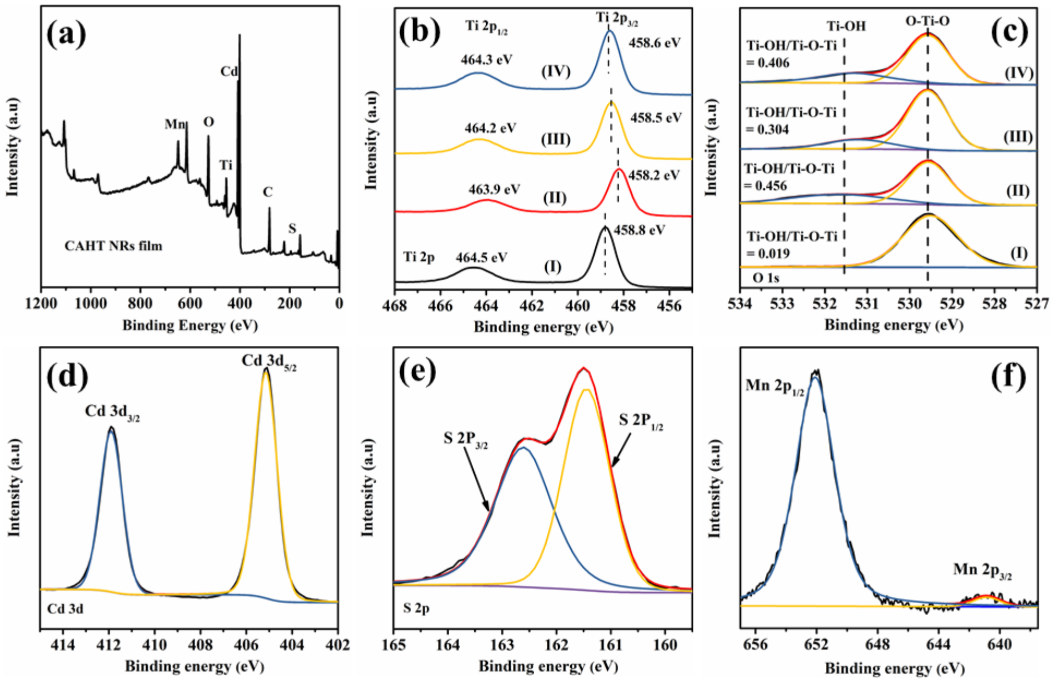

Figure 4. Full scan survey XPS spectrum (a) and exemplified XPS spectra of Ti 2p (b), O 1s (c), Cd 3d (d), S 2p (e) and Mn 2p (f) from quaternary CAHT NRs hybrid composite. A comparison of Ti 2p and O 1s XPS spectra between different samples (TNRs (I), H-TNRs (II), A-H-TNRs (III) and CAHT NRs (IV)) is also listed in (b) and (c), respectively.

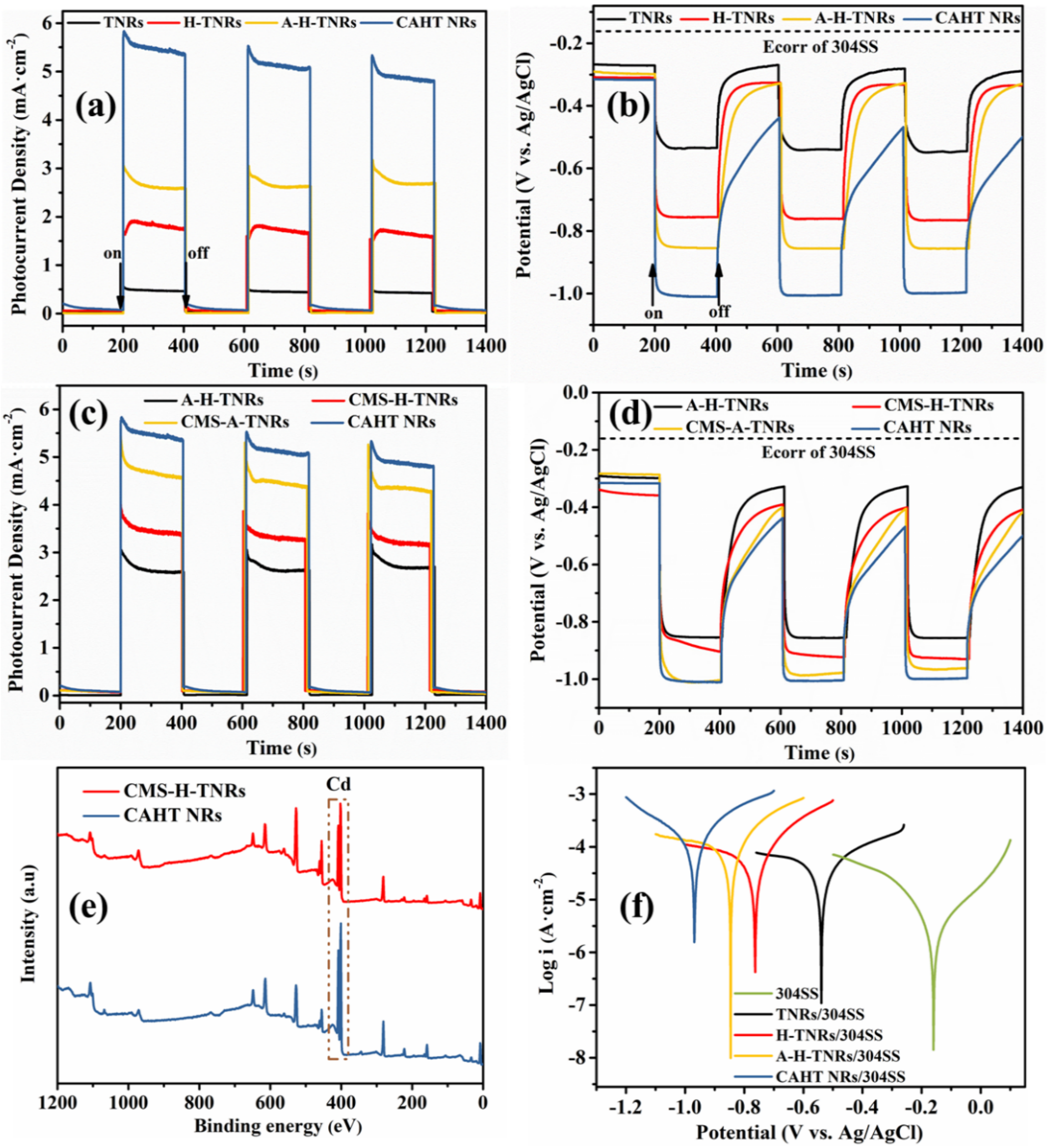

Figure 5. (a and c) The photocurrent responses, (b and d) potential variations, (f) polarization curves between the as-prepared samples in 0.1 M Na_2S and 0.2 M NaOH mixed solution and 304SS electrode in 3.5 wt% NaCl solution under intermittent simulated solar light irradiation. (e) A comparison of full scan survey XPS spectrum between CAHT NRs and CMS-H-TNRs samples.

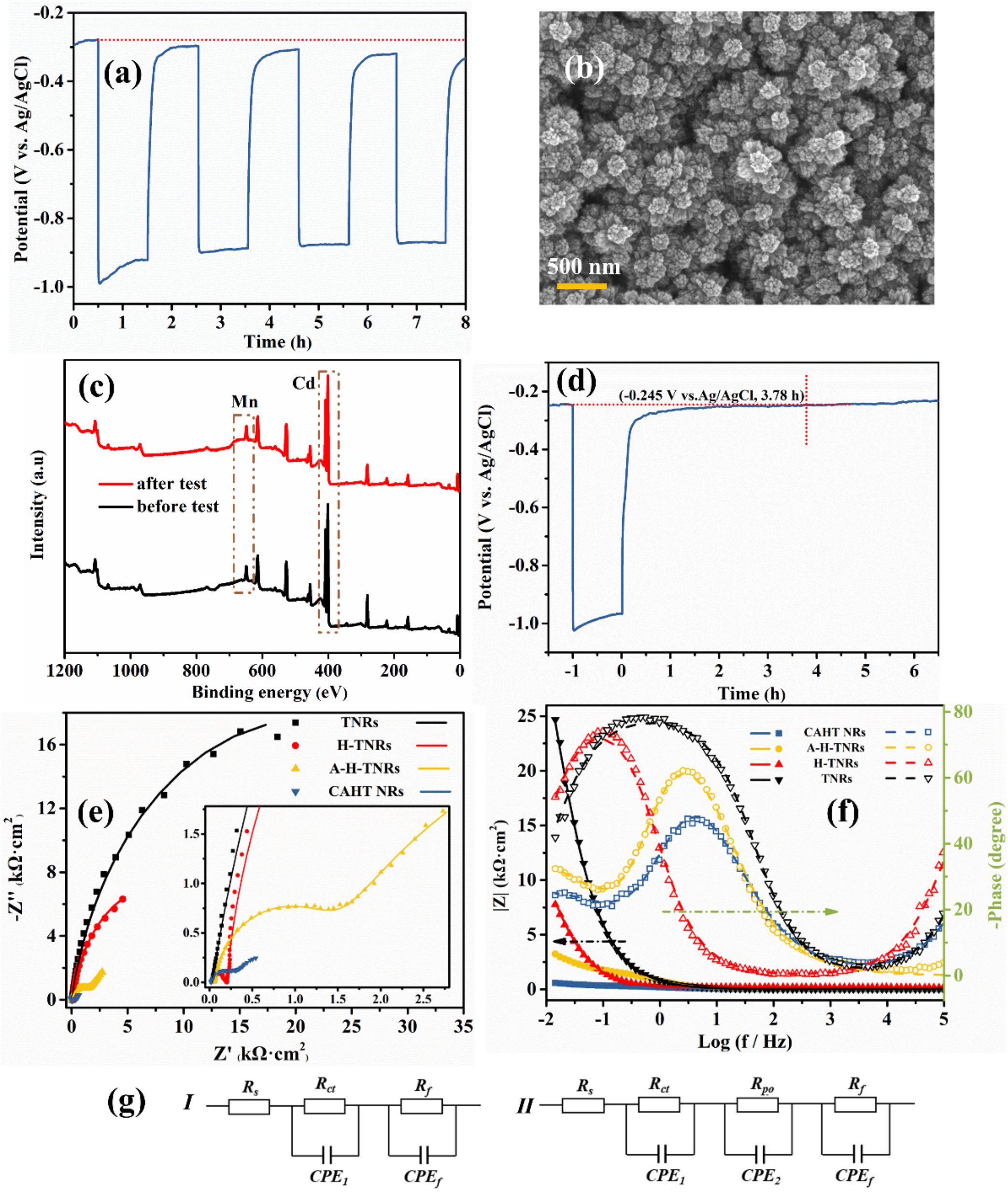

Figure 6. (a) The potential curves of 304SS in 3.5 wt% NaCl solution coupled with this composite film in 0.1 M Na$_2$S and 0.2 M NaOH mixed solution to the light on/off cycles. (b) The SEM images of the AGSQT NRs film after 8 hours' intermittently solar light illumination. (c) A comparison of full scan survey XPS spectrum of the CAHT NRs hybrid composite film before and after 8 hours' PCP test. (d) The time-resolved potential evolution of 304SS in 3.5 wt% NaCl solution coupled with AGSQT NRs hybrid composite film in 0.1 M Na$_2$S and 0.2 M NaOH mixed solution after photoexcitation. (e) Nyquist plots, and (f) Bode-Phase plots of CAHT NRs and each component in 0.5 M Na$_2$SO$_4$ solution under intermittent simulated solar light irradiation. (g) The equivalent circuit for fitting the impedance data.

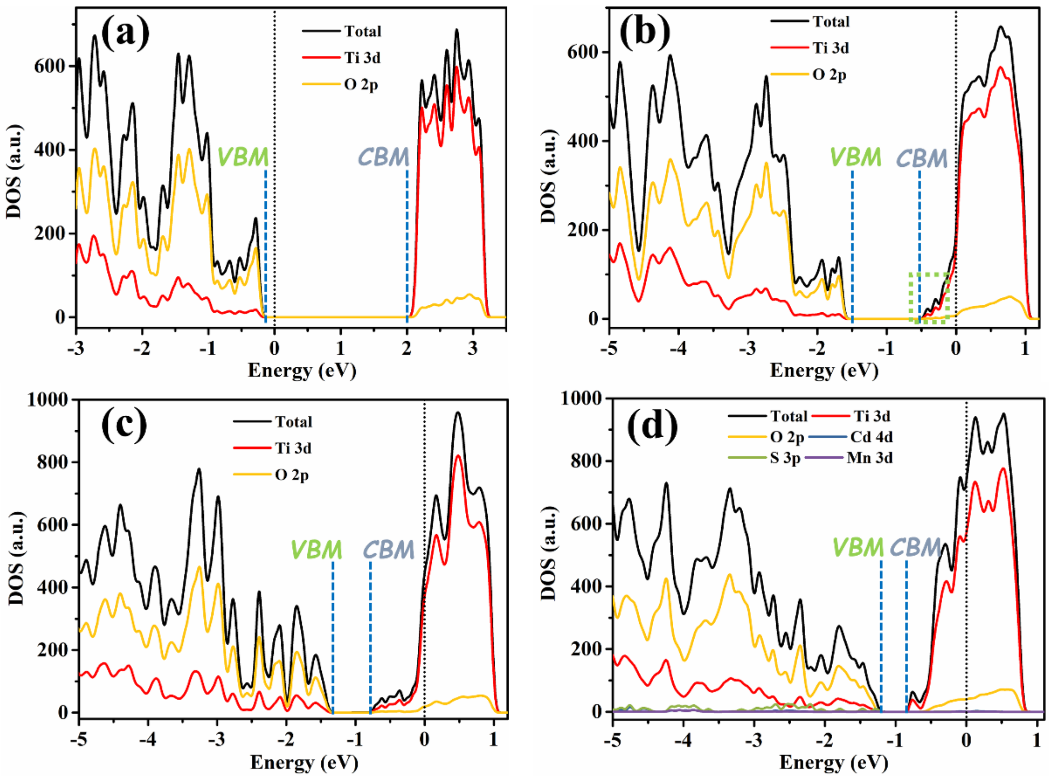

Figure 7. Total and partial electronic density of states (TDOS and PDOS) for TNRs (a), H-TNRs (b), A-H-TNRs (c) and CAHT NRs hybrids (d).

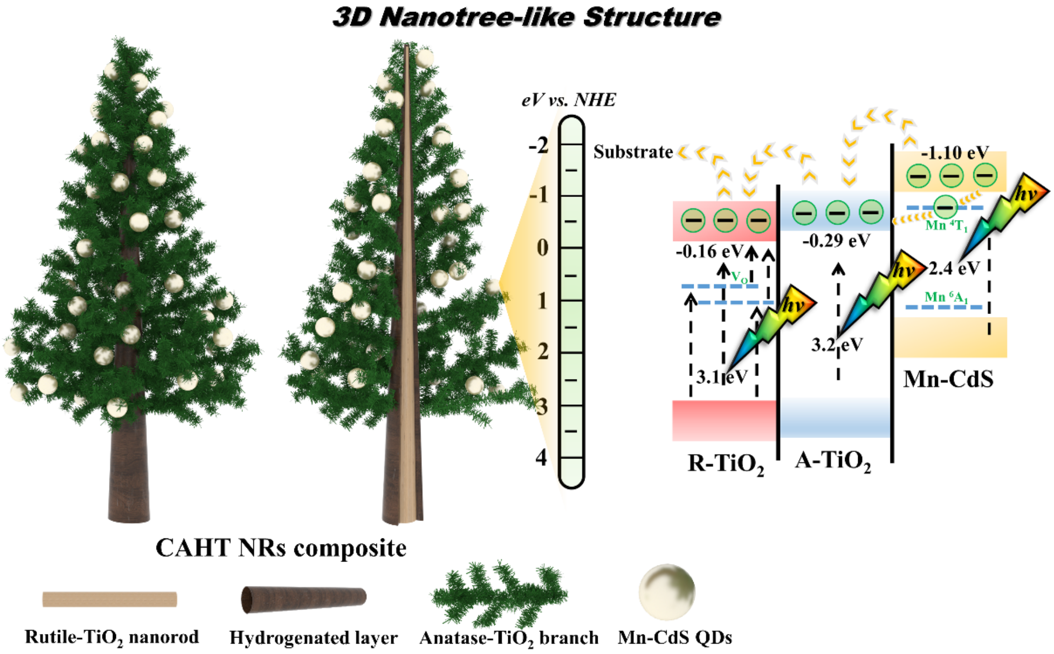

Scheme 2. The schematic and energy level alignment illustrating the as-proposed charge photogeneration and transfer mechanism in the CAHT NRs film enhanced PCP application.

Supporting information

Towards Energy Level Cascaded "Quantum Armours" Combating Metal Corrosion

Yunpeng Liu [a], Jinwei Zhu [a,e], Zhenyu Wang [a], Xuanye Yan [a], Juantao Zhang [a], Wenlong Zhang [a], Hao Xu [a], Frank Marken [b], Jiangtao Feng [a*], Bo Hou [c**], Wei Yan [d***] , Mingtao Li[g], and Zijun Ren [f]

a Department of Environmental Science & Engineering, State Key Laboratory of Multiphase Flow in Power Engineering, School of Energy and Power Engineering, Xi'an Jiaotong University, Xi'an, 710049, China. Email: fjtes@xjtu.edu.cn

b Department of Chemistry, University of Bath, Claverton Down, Bath BA2 7AY, U.K.

c School of Physics and Astronomy, Cardiff University, The Parade, Cardiff, CF24 3AA, Wales, UK. Email: HouB6@cardiff.ac.uk

d State Key Laboratory of Multiphase Flow in Power Engineering, School of Energy and Power Engineering, Xi'an Jiaotong University, Xi'an, 710049, China. Email: yanwei@xjtu.edu.cn

e Shaanxi Electrical Equipment Institute, Xi'an, 710025, China

f Instrument Analysis Center of Xi'an Jiaotong University, Xi'an Jiaotong University, Xi'an, 710049, China

g International Research Center for Renewable Energy (IRCRE), State Key Laboratory of Multiphase Flow in Power Engineering (MFPE), Xi'an Jiaotong University, Xi'an, 710049, China

Corresponding authors:

Jiangtao Feng: fjtes@xjtu.edu.cn

Bo Hou: HouB6@cardiff.ac.uk

Wei Yan: yanwei@xjtu.edu.cn

Supplementary Contents

Experimental details

Materials

Chemicals: Hydrochloric acid (HCl), sodium hydroxide (NaOH), sodium chloride (NaCl), sodium sulphide nonahydrate ($Na_2S·9H_2O$), titanium butoxide ($C_{16}H_{36}O_4Ti$), titanium tetrachloride ($TiCl_4$), cadmium acetate dehydrate ($Cd(CH_3COO)_2·2H_2O$) manganous (II) acetate tetrahydrate ($Mn(CH_3COO)_2·4H_2O$) and methanol were all purchased from Sinopharm Chemical Reagent Co. Ltd (Shanghai, China). All the chemicals were used directly without any purification. Distilled water (DIW) was used in the preparation of all solutions.

FTO glass (7 $\Omega·cm^{-2}$, 2.2 mm-thick) was purchased from Guluo Glass Co. Ltd, (Luoyang, China). The FTO was sequentially cleaned by DIW, acetone and methanol for 30 min in an ultrasonic bath. Finally, these substrates were dried in ambient air.

Characterization

The morphology and microstructure of the as-prepared samples were investigated by scanning electron microscope (SEM Zeiss Gemini SEM 500) and field-emission transmission electron microscopy (TEM, JEOL JEM-F200 (HR)). The x-ray diffraction (XRD) patterns of samples were recorded on a Bruker D8 ADVANCE using Cu Kα radiation (λ=1.5418 Å). The Raman measurement (LabRAM HR Evolution, with an excitation of 325 nm laser light) were used to analyze the composition of samples. The X-ray photoelectron spectroscopy (XPS) spectrums of samples were obtained from a Thermo Scientific EscaLab 250Xi with an Al monochromatic X-ray source (1486.6 eV). All binding energies (BEs) were referenced to the C 1s hydrocarbon peak at 284.8 eV. The optical absorption abilities of the samples were investigated by the absorbance mode of UV-visible diffuse reflectance absorption spectrum (DRS, PE Lambda950).

The photoluminescence (PL) excitation spectra were studied using an Edinburgh FLS9 luminescence spectrofluorophotometer equipped with a Xe lamp presenting an exciting wavelength at 330 nm.

Computational methods

The Vienna Ab Initio Package (VASP) was employed to perform all the density DFT calculations within the generalized gradient approximation (GGA) using the Perdew-Burke-Ernzerhof (PBE) formulation [1, 2]. The projected augmented wave (PAW) potentials were chosen to describe the ionic cores and take valence electrons into account using a plane-wave basis set with a kinetic energy cutoff of 400 eV [3]. Partial occupancies of the Kohn-Sham orbitals were allowed using the Gaussian smearing method and a width of 0.05 eV. The on-site corrections (DFT+U) has been applied to the 3d electron of Ti atoms (U_{eff} = 4.5 eV) [4], 4d electron of Cd atoms (U_{eff} = 4 eV) [5], 3d electron of Mn atoms (U_{eff} = 4.5 eV) [6]. The energy was considered self-consistent when the energy change was smaller than 10^{-5} eV. Geometry optimization was considered convergent when the force change was smaller than 0.02 eV/Å. Grimme's DFT-D3 methodology was used to describe the dispersion interactions [7].

The equilibrium lattice constants of rutile TiO_2 unit cell were optimized, when using a 10×10×16 Monkhorst-Pack k-point grid for Brillouin zone sampling, to be a = b = 4.657 Å and c = 3.014 Å. To accommodate an anatase-TiO_2 and Mn-CdS cluster, a large TiO_2 (1 1 0) surface model was constructed with a p (5x4) periodicity in the x and y directions and two stoichiometric layers (6 atomic layers) of rutile TiO_2 (1 1 0) in the z-directions. A vacuum layer with the depth of 20 Å is used to separate the surface slab from its periodic duplicates. This rutile TiO_2 (1 1 0) surface model contains 132 Ti and 264 O atoms and has the size of 24.462 Å, 17.231 Å and 39 Å in the x, y and z-direction, respectively.

As shown in Figure S15 (Supporting Information), the ratio of Ti^{4+}:Ti^{3+} is determined as approximately 5:1 from the XPS results of H-TNRs samples. Because the XPS results reflect the surface chemical condition of the film [8], one-twelfth oxygen atoms in the upper 3 atomic layers of TiO_2 (1 1 0) are removed to construct the defect structure of H-TNRs.

The equilibrium lattice constants of anatase TiO_2 unit cell were optimized, when using a 9×9×9 Monkhorst-Pack k-point grid for Brillouin zone sampling, to be a = b = c = 5.443 Å. Due to anatase TiO_2 (1 0 1) lattice plane has been widely investigated in the photocatalytic field, a large anatase TiO_2 (1 1 0) surface model was constructed with a p (4x3) periodicity in the x and y directions and one stoichiometric layer (3 atomic layers) of anatase TiO_2 (1 0 1) (40 Ti and 100 O atoms) in the z-directions. To form multiphase heterojunction, VASPKIT software was utilized to place anatase TiO_2 (1 0 1) surface on the top of rutile TiO_2 (1 1 0) surface at a distance of 3 Å [9], and the lattice mismatch rate between substrate and adsorbate was ensured to be less than 1%.

The close-packed double-layered 20%Mn-doped CdS cluster (16 Cd, 20 S atoms and 4 Mn atoms on the top layer) was employed and constructed on top of the anatase-TiO_2 (1 0 1) surface at a distance of 3 Å.

During structural optimizations of the above models (Figure S16, Supporting Information), the gamma point in the Brillouin zone was used for k-point sampling, and the bottom rutile TiO_2 lower 3 atomic layers were fixed at the same time. Then, all the rest of the atoms were allowed to fully relax.

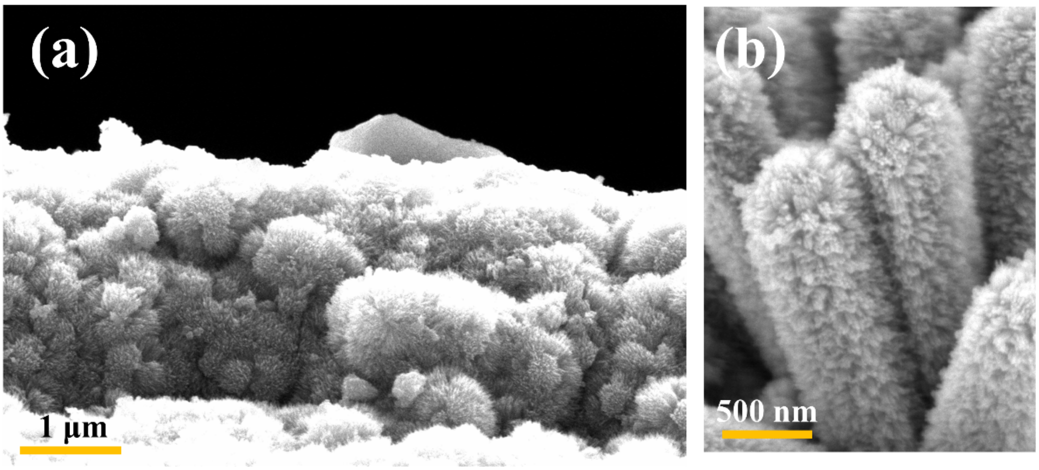

Figure S1. Cross-section SEM images of the CAHT NRs composite film (a and b).

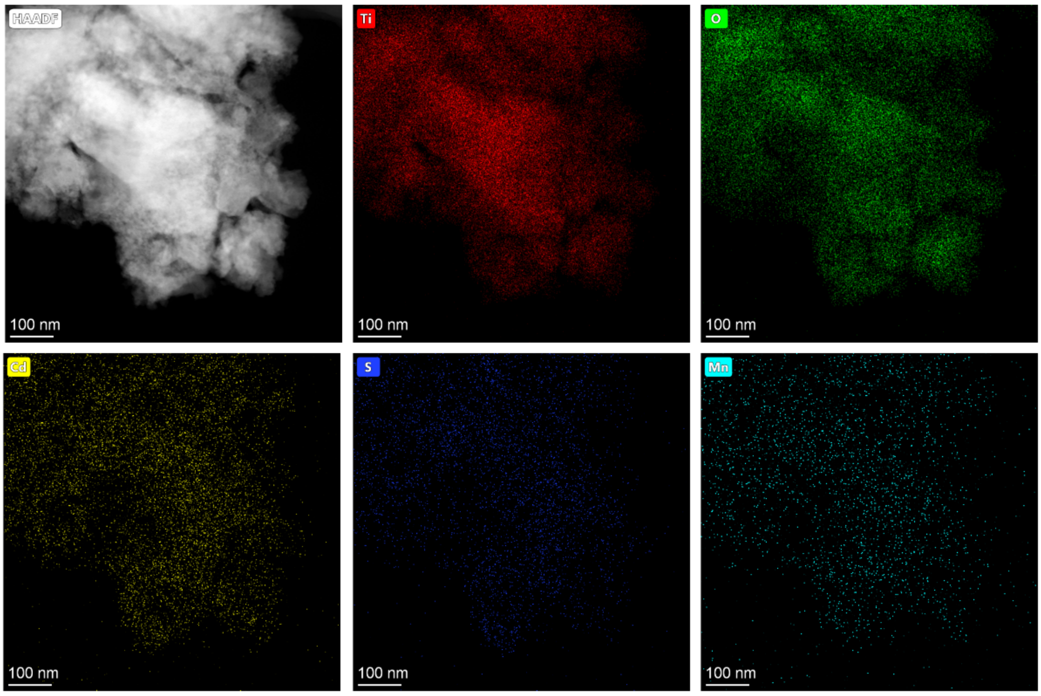

Figure S2. EDS element mapping images of Ti, O, Cd, S and Mn from the selected area of CAHT NRs composite.

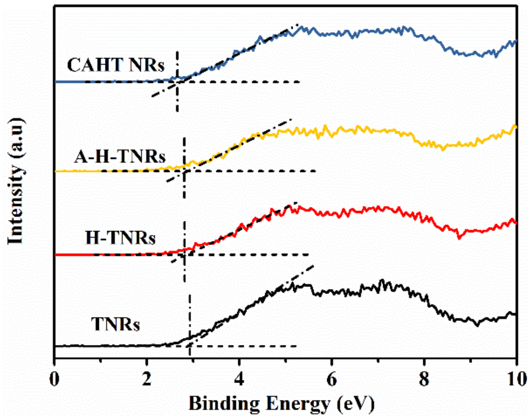

Figure S3. XPS VB spectrum of the as-prepared film.

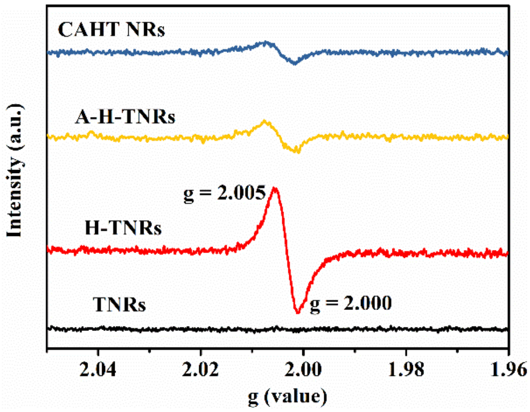

Figure S4. Typical EPR spectra of the as-prepared samples.

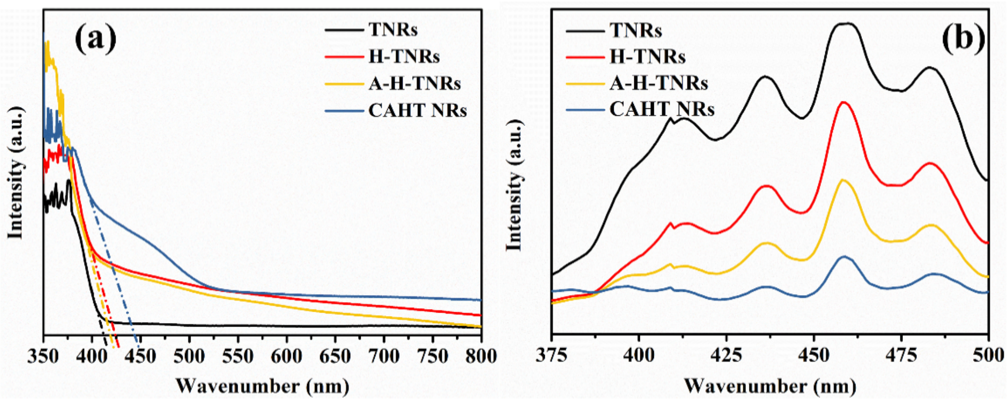

Figure S5. UV-visible diffuse reflectance spectra (a) and PL spectra (b) of quaternary CAHT NRs hybrid composite films.

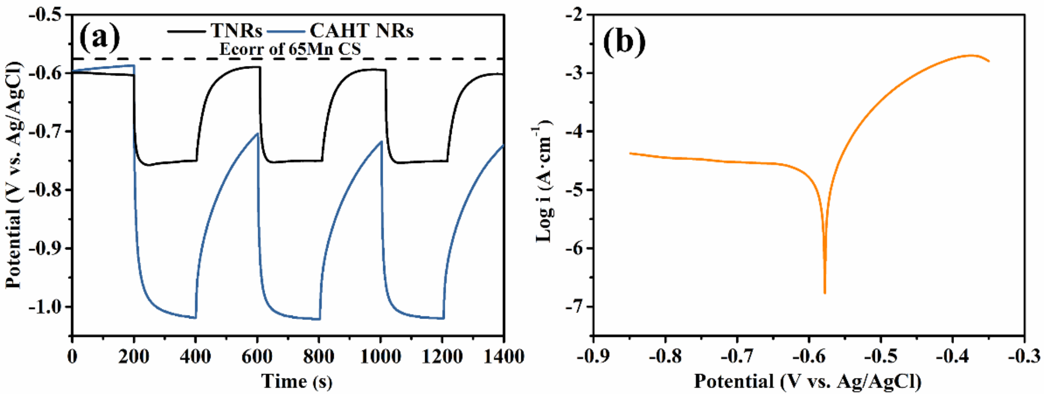

Figure S6. The potential variations (a) between the as-prepared samples in 0.1 M Na_2S and 0.2 M NaOH mixed solution and 65Mn CS electrode in 3.5 wt% NaCl solution under intermittent simulated solar light irradiation; The polarization curves (b) of uncoupled 65Mn CS electrode in 3.5 wt% NaCl solution.

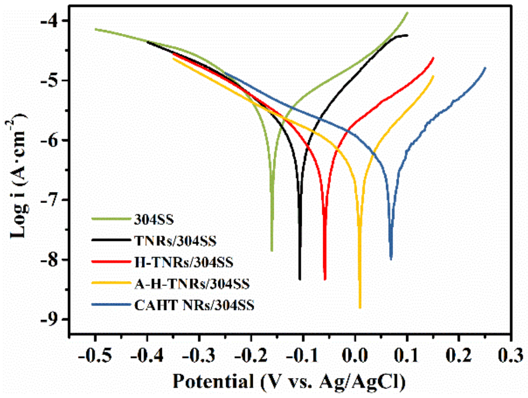

Figure S7. Polarization curves of bare 304SS, and 304SS in 3.5 wt% NaCl solution coupled with different photoanodes in 0.1 M Na_2S and 0.2 M NaOH mixed solution in the dark condition.

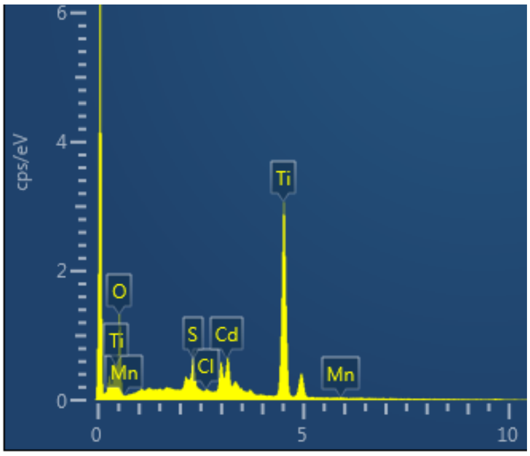

Figure S8. EDS spectrum of CAHT NRs after 8 hours' PCP test

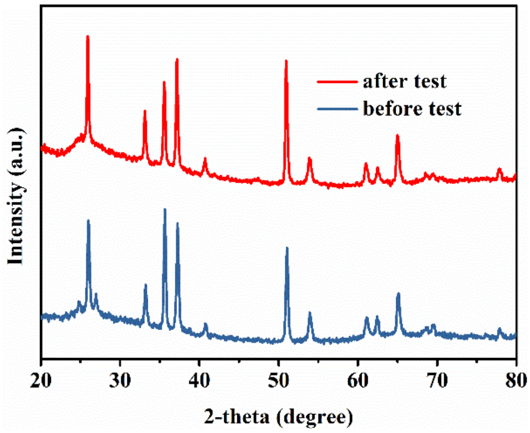

Figure S9. The XRD spectrum of the CAHT NRs hybrid composite film before and after 8 hours' PCP test.

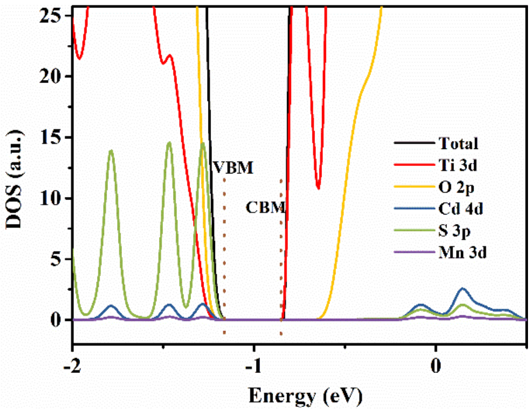

Figure S10. Partial electronic density of states for CAHT NRs hybrids.

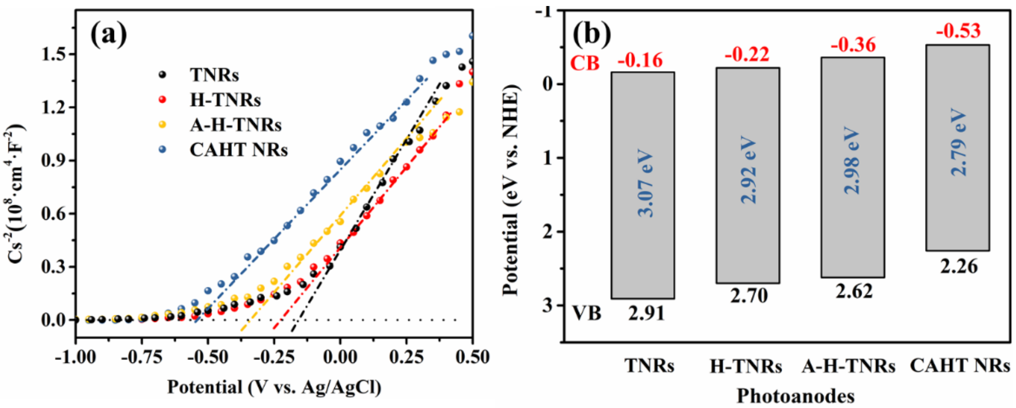

Figure S11. Mott-Schottky plots(three-electrodes cell employing 0.5 M Na_2SO_4 solution) (a) and relative changes of the CB, Fermi and VB positions (b) of as-prepared films.

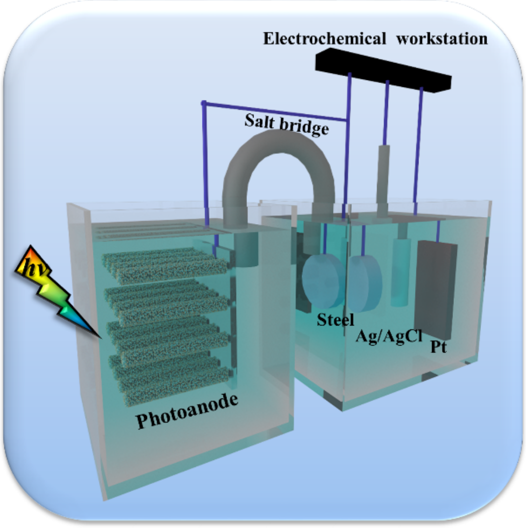

Figure S12. Schematic of the photoelectrochemical test configuration

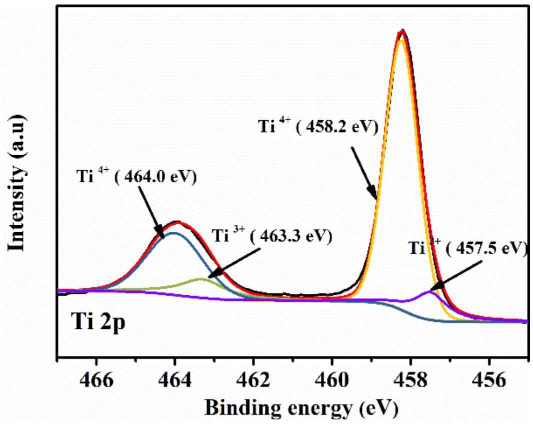

Figure S13. The XPS Ti 2p core-level spectrum of the H-TNRs film.

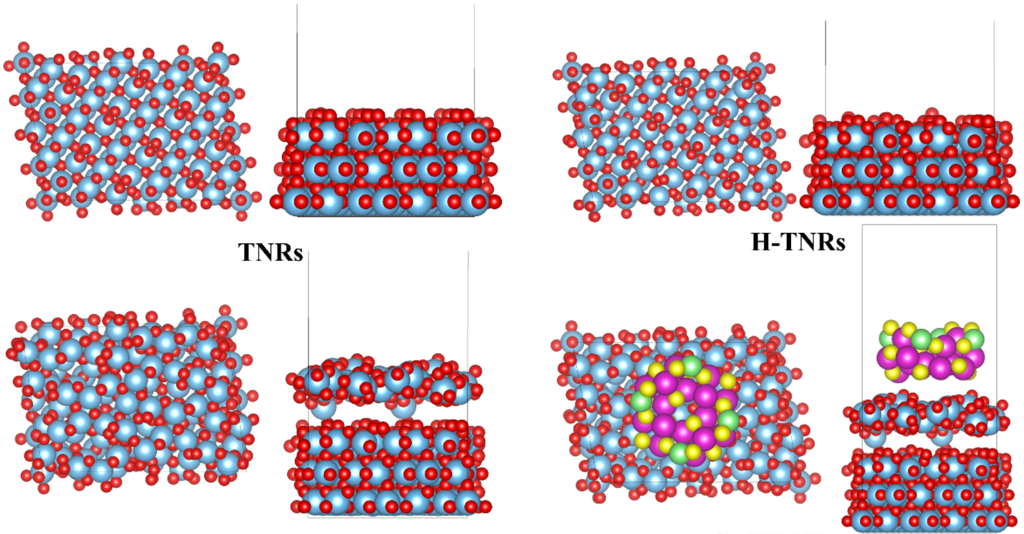

TNRs

H-TNRs

A-H-TNRs

CAHT NRs

Figure S14. Space-filing structural models of as-prepared films from the top and side views. (Ti: blue, O: red, Cd: violet, S: yellow, Mn: green)

Table S1. Comparison of previously reported catalysts for photocathodic protection.

Samples	Corrosive medium	Electrochemical cell medium	Light source	Metal	OCP drop	Ref
ZnS-Bi_2S_3/TiO_2/WO_3 composite film	0.5 M NaCl	0.1 M Na_2S + 0.1 M Na_2SO_3 mixed solution	150 W Xe lamp; white light	304SS	540 mV	[10]
$MgIn_2S_4$/TiO_2 composite film	3.5 wt% NaCl	0.1 M Na_2S + 0.2 M NaOH mixed solution	300 W Xe lamp; visible light	Q235 CS	420 mV	[11]
Ag@$CuFe_2O_4$@TiO_2 nanocomposite film	3.5 wt% NaCl	0.25 M Na_2SO_3	300 W Xe lamp; visible light	304SS	485 mV	[12]
CdSe/$ZnIn_2S_4$ modified TiO2 nanotube composite	0.5 M NaCl	0.1 M Na_2S + 0.1 M Na_2SO_3 mixed solution	150 W Xe lamp; white light	403SS	240 mV	[13]
nanoflower like SnO_2-TiO_2 nanotubes composite photoelectrode	3.5 wt% NaCl	0.1 M NaOH	300 W Xe lamp; UV light	304SS	400 mV	[14]
carbon quantum dots/Ag sensitized TiO_2 nanotube film	0.5 M NaCl	0.5 M Na_2SO_4	150 W Xe lamp; white light	403SS	400 mV	[15]
Bi_2S_3 nanoparticles/ZnO nanowire heterojunction films	3.5 wt% NaCl	0.1 M Na_2S + 0.2 M NaOH mixed solution	300 W Xe lamp; visible light	304SS	430 mV	[16]
heterostructured β-Bi_2O_3-TiO_2 nanotube array composite film	0.5 M NaCl	0.5 M Na_2SO_4	150 W Xe lamp; white light	403SS	510 mV	[17]
TiO_2-$BiVO_4$-CdS film	3.5 wt% NaCl	3.5 wt% NaCl	300 W Xe lamp; white light	304SS	230 mV	[18]
quaternary CAHT NRs hybrid composite superstructure	3.5 wt% NaCl	0.1 M Na_2S + 0.2 M NaOH mixed solution	500 W Xe lamp; simulated solar light	304SS	684 mV	This work
quaternary CAHT NRs hybrid composite superstructure	3.5 wt% NaCl	0.1 M Na_2S + 0.2 M NaOH mixed solution	500 W Xe lamp; simulated solar light	65Mn CS	416 mV	This work

Table S2. Derivative parameters obtained by fitting the impedance data.

Samples	R_s ($\Omega\cdot cm^2$)	CPE_f		R_f ($k\Omega\cdot cm^2$)	CPE_2		R_{po} ($k\Omega\cdot cm^2$)	CPE_1		R_{ct} ($k\Omega\cdot cm^2$)
		Y_f ($S\cdot cm^{-2}\ s^{-n}$)	n_f		Y_{01} ($S\ cm^{-2}\ s^{-n}$)	n_2		Y_{02} ($S\ cm^{-2}\ s^{-n}$)	n_1	
TNRs	15.63	1.56×10^{-4}	0.85	0.30	—	—	—	2.46×10^{-4}	0.88	42.38
H-TNRs	25.19	4.65×10^{-5}	0.86	0.20	—	—	—	9.96×10^{-5}	0.93	15.89
A-H-TNRs	48.66	5.86×10^{-3}	0.91	22.20	2.32×10^{-4}	0.96	1.23	9.59×10^{-5}	0.80	8.27
CMS-A-H-TNRs	10.01	7.27×10^{-3}	0.91	1.76	5.79×10^{-7}	0.88	0.18	2.02×10^{-3}	0.90	0.19

Reference

[1] G. Kresse, J. Furthmüller, Efficiency of ab-initio total energy calculations for metals and semiconductors using a plane-wave basis set, Comput. Mater. Sci. 1996;6:15-50.

[2] G. Kresse, J. Furthmüller, Efficient iterative schemes for ab initio total-energy calculations using a plane-wave basis set, Phys. Rev. B, 1996;54:11169-11186.

[3] P.E. Blochl, Projector augmented-wave method, Phys Rev B Condens Matter 1994;50:17953-17979.

[4] S.L. Dudarev, G.A. Botton, S.Y. Savrasov, C.J. Humphreys, A.P. Sutton, Electron-energy-loss spectra and the structural stability of nickel oxide: An LSDA+U study, Phys. Rev. B, 1998;57:1505-1509.

[5] J.I. Khan, Z.K. Khan, M.N. Usmani, Shift in optical properties of Mn doped CdS (A DFT+U study), Mater. Res. Express 2018;5:015915.

[6] O. Dialessandro, D. Garcia Pintos, A. Juan, B. Irigoyen, J. Sambeth, A DFT study of phenol adsorption on a low doping Mn–Ce composite oxide model, Appl. Surf. Sci. 2015;359:14-20.

[7] S. Grimme, J. Antony, S. Ehrlich, H. Krieg, A consistent and accurate ab initio parametrization of density functional dispersion correction (DFT-D) for the 94 elements H-Pu, J. Chem. Phys. 2010;132:154104.

[8] C. Passiu, A. Rossi, M. Weinert, W. Tysoe, N.D. Spencer, Probing the Outermost Layer of Thin Gold Films by XPS and Density Functional Theory, Appl. Surf. Sci. 2019;507:145084.

[9] V. Wang, N. Xu, J.C. Liu, G. Tang, W.T. Geng, VASPKIT: A User-friendly Interface Facilitating High-throughput Computing and Analysis Using VASP Code, *Comput. Phys. Commun.* 2019;267:1080332] G. Kresse, J. Furthmüller, Efficient iterative schemes for ab initio total-energy calculations using a plane-wave basis set, Physical Review B, 54 (1996) 11169-11186.

[10] Z.C. Guan, X. Wang, P. Jin, Y.Y. Tang, H.P. Wang, G.L. Song, R.G. Du, Enhanced photoelectrochemical performances of ZnS-$Bi_2S3/TiO_2/WO_3$ composite film for photocathodic protection, Corros. Sci., 143 (2018) 31-38.

[11] H. Li, X. Cui, W. Song, Z. Yang, Y. Li, P. Zhang, Z. Zheng, Y. Wang, J. Li, F. Ma, Direct Z-scheme $MgIn_2S_4/TiO_2$ heterojunction for enhanced photocathodic protection of metals under visible light, Nanotechnology, 33 (2022).

[12] N. Wang, J. Wang, M. Liu, C. Ge, B. Hou, Y. Ning, Y. Hu, Preparation of Ag@$CuFe_2O_4$@TiO_2 nanocomposite films and its performance of photoelectrochemical cathodic protection, J. Mater. Sci. Technol., 100 (2022) 12-19.

[13] P. Jin, Z.C. Guan, H.-P. Wang, X. Wang, G.L. Song, R.G. Du, Fabrication of CdSe/$ZnIn_2S_4$ modified TiO2 nanotube composite and its application in photoelectrochemical cathodic protection, J. Electroanal. Chem., 904 (2022).

[14] J. Zhang, Z. Ur Rahman, Y. Zheng, C. Zhu, M. Tian, D. Wang, Nanoflower like SnO_2-TiO_2 nanotubes composite photoelectrode for efficient photocathodic protection of 304 stainless steel, Appl. Surf. Sci., 457 (2018) 516-521.

[15] Z.C. Guan, P. Jin, Q. Liu, X. Wang, L.F. Chen, H. Xu, G.L. Song, R.G. Du, Carbon quantum dots/Ag sensitized TiO_2 nanotube film for applications in photocathodic protection, J. Alloys Compd., 797 (2019) 912-921.

[16] Y. Zhang, H. Bao, X. Liu, X. Zhang, H. He, T. Li, H. Yang, S.P. Shah, W. Li, Bi2S3 nanoparticles/ZnO nanowire heterojunction films for improved photoelectrochemical cathodic protection for 304 SS under visible light, J. Appl. Electrochem., 52 (2022) 559-571.

[17] Z.C. Guan, H.P. Wang, X. Wang, J. Hu, R.G. Du, Fabrication of heterostructured β-Bi_2O_3-TiO_2 nanotube array composite film for photoelectrochemical cathodic protection applications, Corros. Sci., 136 (2018) 60-69.

[18] W. Li, L. Wei, T. Shen, Y. Wei, K. Li, F. Liu, W. Li, Ingenious preparation of “layered-closed” TiO_2-$BiVO_4$-CdS film and its highly stable and sensitive photoelectrochemical cathodic protection performance, Chem. Eng. J., 429 (2022).